Journal of Sailing Technology 2024, volume 9, issue 1, pp. 143 - 174.
The Society of Naval Architects and Marine Engineers.

AC75 Aerodynamic Performance Prediction via BEM

Michele Francesco Melis
Hamburg University of Technology, Germany, michele.melis@tuhh.de.

Rafael Tannenberg
University of Southampton, United Kingdom.

Stephen Boyd
University of Southampton, United Kingdom.

Moustafa Abdel-Maksoud
Hamburg University of Technology, Germany.

Manuscript received November 15, 2024; revision received December 14, 2024; accepted December 19, 2024.

LRPP LEQ12 sailing in Cagliari, Sardinia (37th Americas´s Cup, Recon © Ivo Rovira)

Abstract. The AC75 class, used in the America's Cup, is a hydro-foiling racing sailing yacht powered by a double-skin main sail and a single-skin jib. The boat performance is typically predicted by a Velocity Prediction Program (VPP). The aerodynamics are usually modeled with surrogate models of data points collected either through wind tunnel experiments, numerical simulations, or empirical formulations. Previous work has shown that empirical models are not able to predict accurate performance as the sailors can efficiently control the flying shape of each sail. In addition, the empirical coefficients are limited to traditional sails, not yet available for a double-skin main, neglecting also the hull shape and its influence on the sails airflow. To achieve more realistic results through the inclusion of hull shape with realistic sail geometries and shape ranges, a compromise must be found between total computational effort and physical simplifications. Reynolds Averaged Navier-Stokes (RANS) methods typically provide accurate predictions but come with a high computational effort. Potential flow-based methods, also used by America's Cup teams, are computationally less expensive while showing some limitations at higher angles of attack with flow separation. Due to the high number of simulations required for a surrogate model at the early design stage, a Boundary Element Method (BEM) was considered appropriate for the task in combination with a RANS method for comparison. Results have shown that the BEM is able to predict reasonable forces generated by the single-skin jib and double-skin main. The performance deltas with endplated sails on the hull with attached vortices, comply with expected trends.

Keywords: AC75; aerodynamics; double-skin; hull; parametric trim; panel code; response surfaces

NOMENCLATURE

A	Substitution coefficient potential source [-]
A_{OA}	Angle of attack [°]
A_{WA}	Apparent wind angle [°]
A_{WS}	Apparent wind speed [m s^{-1}]
B	Substitution coefficient potential doublet [-]
C_{FX}	Aerodynamic drive force coefficient [-]
C_{FY}	Aerodynamic side force coefficient [-]
C_{FZ}	Aerodynamic vertical force coefficient [-]
C_{D}	Aerodynamic drag force coefficient [-]
C_{L}	Aerodynamic lift force coefficient [-]
C_{MX}	Aerodynamic heel moment coefficient [-]
C_{MY}	Aerodynamic pitch moment coefficient [-]
C_{MZ}	Aerodynamic yaw moment coefficient [-]
C_{P}	Pressure coefficient [-]
∂	Partial derivative operator [-]
d_{Z}	Ride height [m]
$\boldsymbol{f}$	Force vector [N]
g	Gravitational acceleration [m s^{-2}]
J_{HR}	Jib head rotation position [-]
J_{TV}	Jib traveler position [-]
k	Constant pressure [Pa]
M_{HR}	Main head rotation position [-]
M_{RA}	Mast rotation angle [°]
M_{TV}	Main traveler position [-]
$\boldsymbol{n}$	Normal direction vector [-]
n_{B}	Body panels [-]
n_{W}	Wake panels [-]
p	Pressure [Pa]
r	Distance [m]
S	Surface [m^2]
S_B	Body surface [m^2]
S_W	Wake surface [m^2]
T_{WA}	True wind angle [°]
T_{WS}	True wind speed [m s^{-1}]
t	Time step [s]
$\boldsymbol{u}$	Motion velocity vector [m s^{-2}]
V_S	Boat speed [m s^{-1}]
V_{MG}	Velocity made good [m s^{-1}]
x	Distance [m]
y^{+}	Undimensional wall distance [-]
γ	Cant Angle [°]
δ_e	Elevator angle [°]
δ_f	Flap angle [°]
δ_r	Rudder angle [°]
Δ	Nabla operator [-]
θ	Pitch angle [°]
λ	Leeway angle [°]
μ	Doublet strength [s^{-1}]
$\mu_{b,ij}$	Doublet strength on body panels [s^{-1}]

$\mu_{w,ij}$	Doublet strength on wake panels [s^{-1}]
ρ	Air density [kg m^{-3}]
σ	Source strength [s^{-1}]
σ_{ij}	Source strength on body panels [s^{-1}]
τ	Flat parameter [-]
τ_m	Reynolds-averaged molecular stress tensor [Pa]
τ_t	Reynolds stress tensor due to averaging [Pa]
ϕ	Heel angle [°]
ϕ_e	External potential [m s^{-1}]
ϕ_i	Induced potential [m s^{-1}]
ϕ_∞	Free stream Potential [m s^{-1}]
Φ	Velocity potential [m s^{-1}]

2D	Two-Dimensional
3D	Three-Dimensional
AC	America's Cup
BEM	Boundary Element Method
CAD	Computer-Aided Design
CFD	Computational Fluid Dynamics
COE	Center Of Effort
DNV	Der Norske Veritas
ETNZ	Emirates Team New Zealand
FDS	Fluid Dynamics Ship Theory
FEM	Finite Element Method
FSI	Fluid Structure Interaction
GUI	Graphical User Interface
IMS	International Measurement System
LRPP	Luna Rossa Prada Pirelli
RANS	Reynolds Averaged Navier-Stokes
SST	Shear Stress Transport
VLM	Vortex Lattice Method
VPP	Velocity Prediction Program

1 INTRODUCTION

Ever since the America‘s Cup (AC) classes have adopted hydro-foiling configurations, the need for accurate numerical tools and prediction software has increased and requires the coupling of all six degrees of freedom. A widely used tool is the Velocity Prediction Program (VPP), estimating the performance of a sailing yacht given certain boat model and environmental data. To rapidly predict the yacht's performance, the VPP utilizes methods usually based on theoretical considerations, experimental data and semi-empirical or numerical methods (Melis et al., 2022). Large aerodynamic coefficient matrices are required to cover the aerodynamic aspects of America´s Cup racing yachts (Collie et al., 2015); hence, potential-based methods are often employed at the early design stage to cover the entire design space.

This paper addresses the challenges of predicting the aerodynamic performance of an AC75 sailing yacht for several sail shapes including the hull influence on sail performance. Specifically the generation of aerodynamic coefficients for improving the accuracy of a previously developed AC75 VPP. A number of considerations were made to achieve the aerodynamic model of the AC75. Firstly, should the method be developed directly within the VPP or externally where the aerodynamics are provided to the VPP using surrogate models. The first option requires developing a module able to couple a 2D strip approach for both sails along span sections and to couple these with a lifting line for the three-dimensional effects. By doing so a robust balance can be achieved between efficiency and accuracy. Similar approaches were used in Birch-Tomlinson et al. (2022), Morvan and Sacher (2021) and Graf et al. (2016). However, this approach neglects effects such as cross-flow, end-plating and is a poor model for main and jib interaction. Developing this method internally to the VPP, would perhaps overload the software with computational effort loosing some efficiency on its rapid search for equilibrium and optimum boat setup. For these reasons, the second option has been taken forward, to develop a method external of the VPP software for more flexibility and accuracy. Considering the significant geometrical differences between the double-skin main and the single-skin jib, the second consideration is the numerical method to be employed. A well-known technique for modeling thin single-skin sails with negligible thickness is the Vortex Lattice Method (VLM) (Katz and Plotkin, 1991). For the double-skin main a more suitable method is a panel Boundary Element Method (BEM) (Katz and Plotkin, 1991) considering its thickness given by the mast section. In the authors' view, several AC teams have developed a framework coupling a BEM for the main with a VLM for the jib, both solved as a combined matrix in one equation system. This approach has been considered for application within the university in-house panel method *pan*MARE (Institute of Fluid Dynamics and Ship Theory, 2020), but due to its complexity it will be considered in the present research. Instead, the BEM code has been used for the main, as a thick airfoil including mast and skins, and for the jib, reducing its thickness to a realistic minimum after running several validation test cases. These are fundamental as this is the first use of this BEM code for such very thin lifting surfaces. With the motivation of improving the sail force accuracy, a parametric model was developed generating a significant number of sail shapes. To obtain sail coefficients that are closer to reality, the hull body of an AC75 was also incorporated into the BEM model to study its influence on these coefficients.

1.1 The AC75

The AC75 class has been introduced for the 36th AC edition. It is a hydro-foiling mono-hull sailing yacht with a fully submerged leeward hydrofoil and lifted windward hydrofoil, both providing the required righting moment. The total drive force is provided by a high-performance adjustable sail plan with a double-skin mainsail hoisted along a profiled rotating mast paired to a classic single-skin thin jib. The hull is defined by the deck and hull lines. The platform geometry plays a significant role in endplating the sails and reducing the air gap between the hull and the free-surface. Endplating means reducing pressure leaks between windward and leeward sides of the sails and by avoiding any tip vortices giving less induced drag.

Figure 1. LRPP single-skin jib and double-skin main © Carlo Borlenghi.

To modify the flying shape of each sail, several shape controls are powered by a hydraulic system charged by cyclors or grinders and utilized by the sailors onboard. The approximate sail area of the main and jib are 140 and 60-90 m^2, respectively. The mast is approximately 26.5 m long and its D-section measures 650 mm in length and 400 mm in width (America´s Cup, 2021). The mast can be bent to change the shape of the mainsail by opening or closing the leech. The mast can rotate around its pin located on deck to control the flow entry angle. The mainsheet controls the twist angle of the main, crucial for power and boat balance. The main cunningham controls the tensions in the main luff while the two outhauls are used to tension or release the main foot adjusting the depth and curvature. The main traveler mainly adjusts its angle of attack and hence the heel balance. The jib is hoisted on the jib halyard running along the forestay. To trim the jib, the sailors can adjust the cunningham to increase or decrease tension, the jib sheet for optimum angle and depth and the jib traveler for the angle of attack and twist profile.

1.2 State of the Art

Aerodynamic coefficients of the sails can be obtained from model scale experiments in a wind tunnel or via sail force dynamometer on the full scale yachts as presented in Masuyama et al. (2009) and Hansen et al. (2007). Recently, with large computational resources available, the design of a high-performance AC sail follows a strict timeline employing high- and low-fidelity numerical tools across different design iterations as presented by Collie et al. (2015) for the AC72 rigid mainsail. The results were validated via wind tunnel experiments for scaled models before the regulations prohibited their use in the following AC campaigns increasing even more the use of computational design. This has encouraged the use of only numerical methods instead of wind tunnel experiments within this project. The VPP requires aerodynamic coefficients in six degrees of freedom covering a number of trim parameters and environmental conditions, confirmed by Collie et al. (2015). More insights on the usage of surrogate models within VPPs reducing the computational cost of creating aerodynamic curves for new and existing sail designs were given by Peart et al. (2021) and Peart et al. (2022). These underline the important use of surrogate models to predict a relatively large spectrum of aerodynamic coefficients. An example of employing a low-fidelity and computationally efficient method instead of time-consuming RANS methods to generate aerodynamic data for a rigid AC50 wing and optimize its flying shape is presented by Birch-Tomlinson et al. (2022). In the latter the need for a parametric sail model is shown, which has also been considered in this project. From a number of sail trims, one is chosen by the VPP based on certain criteria. This important search for optimum sail trim and design of traditional thin sails is treated in Rousselon (2020) using a finite volume RANS solver. Recent studies on aerodynamic force coefficient predictions of main wing sails combined to thin jib foresails using numerical methods in the same solver are presented in Grassi et al. (2013). The use of these predictions directly within VPPs as surrogate models is reported in Graf et al. (2016). The fundamental need of VPPs for foiling classes, by means of six degrees of freedom, is presented by Patterson and Binns (2022) for an AC75 and by Melis et al. (2022) where static VPPs were developed based on simple theories and assumptions. The application of VPPs for hydrofoil optimization applied to the AC75 appendages was presented in Tannenberg et al. (2023) and Tannenberg et al. (2024) underlining also the importance of accurate aerodynamic data to identify the correct optimum hydrofoil candidate. Insights on dynamic behaviors and balance with sail trim controls of foiling AC classes were given by Rodriguez et al. (2022) for an AC75 take-off sequence and by Hansen et al. (2019) for an AC50 maneuver optimization. For these VPPs, the aerodynamic forces and moments were modeled by importing large and computationally expensive data matrices that were generated by higher fidelity methods. It is also known, that the performance of any foiling sailing yacht is optimized with VPPs while its dynamic behavior is often studied employing simulators, which are fed with simulation data. As for the structural properties of loaded sails, a specific analysis has been presented by Smith and Wright (2021) and Smith and Wright (2022) on rigid and aero-elastostatic characteristics and equilibrium sail shapes of the AC75 mast and double-skin mainsails. A simulation was run for a specific trim without a jib sail using a Computational Fluid Dynamic (CFD) code with a Finite Element Method (FEM) to model the Fluid Structure Interaction (FSI). This interaction has also been studied by Morvan and Sacher (2021) modeling FSI for thin yacht sails including the crucial interaction between mainsail and jib. Considering the aerodynamic package of AC75 sails and hull, several studies on the airflow vortices and forces generated by the hull body in certain sailing conditions are presented in Gambacciani (2021). These certainly motivate the inclusion of the hull body in the BEM model.

2 PARAMETRIC MODEL

Ideally, to generate realistic flying shapes considering structural limits, such as maximum outhaul, halyard, cunningham, and sheet loads, an FSI solver would be the most appropriate. This has been shown by Smith and Wright (2022) confirming the difference between elastic and rigid performances of a double-skin mainsail. However, accounting for all the structural properties has been considered beyond the scope of the here-developed methodology. For this project and considering it part of an earlier design stage, a large amount of sail shapes are generated and analyzed under the assumption of no deformation. Considering this approach, mirroring all the different sail trim controls was not feasible, and therefore some simplifications were required to reduce the number of trim combinations. Even if only fully foiling sailing conditions are targeted, a parametric model is necessary. A simplified CAD-based parametric model has been developed in Rhino3D-Grasshopper using B-spline curves with adjusted knots and weights of control points to reproduce a vast number of sail shapes by adjusting virtual trim controls. The rig geometries and sail shapes have been taken from the official class regulation (Royal-New-Zealand-Yacht-Squadron-and-Royal-Yacht-Squadron, 2022) and by broadcast footage (America´s Cup, 2021) for the 7th match race of the 36th AC edition. It was chosen based on its T_{WA} and T_{WS} consistency (11 kn). Hull lines of an AC75 yacht similar to the previous ETNZ boat were drawn based on Chevalier and Taglang (2021) as displayed in Figure 2. The mast was raked aft by 5 degrees. Heel and pitch angles differential are only considered in the simulation of sails and hull platform while for sails only these are set to 0 degrees. For the double-skin main, virtual trim controls such as mast rotation angle M_{RA}, main traveler (M_{TV}), and main head rotation (M_{HR}) were defined. For the jib, the jib traveler (J_{TV}) and jib head rotation (J_{HR}), were defined, as shown in Figure 2.

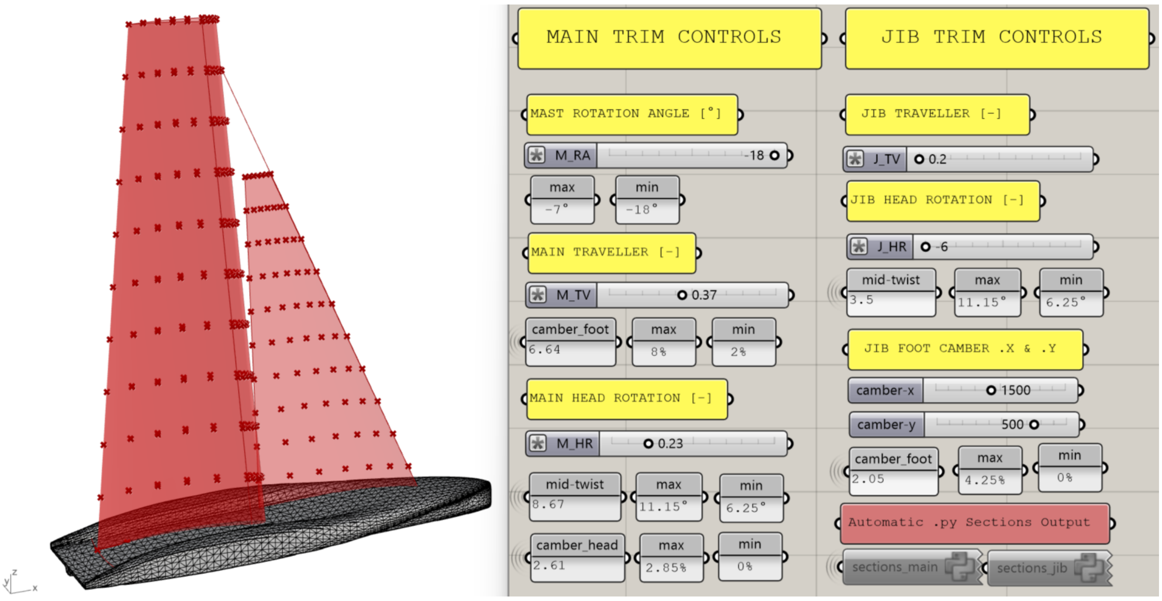

MAIN TRIM CONTROLS

MAST ROTATION ANGLE [°]
M_RA -18
max -7°
min -18°

MAIN TRAVELLER [-]
M_TV 0.37
camber_foot 6.64
max 8%
min 2%

MAIN HEAD ROTATION [-]
M_HR 0.23
mid-twist 8.67
max 11.15°
min 6.25°
camber_head 2.61
max 2.85%
min 0%

JIB TRIM CONTROLS

JIB TRAVELLER [-]
J_TV 0.2

JIB HEAD ROTATION [-]
J_HR -6
mid-twist 3.5
max 11.15°
min 6.25°

JIB FOOT CAMBER .X & .Y
camber-x 1500
camber-y 500
camber_foot 2.05
max 4.25%
min 0%

Automatic .py Sections Output
sections_main
sections_jib

Figure 2. Hull geometry, sail sections and trim control sliders.

All sliders except M_{RA}, are dimensionless and parameterized in ranges [0:1] considering the length of the green curves, by means of main and jib tracks, shown in Figure 3. In black color are the undeformed and symmetrical profiles of main and jib, in red the 2D parametric sail shapes and in blue the apparent wind angle A_{WA} convention. For a matter of simplicity, the maximum jib position has been set constant at a specific chord length and draft adjusted based on A_{WA} for an appropriate entry angle. Also, the M_{RA} parameter is set as a function of the A_{WA}, either equal or smaller by -2 degrees. For the main, the foot and head drafts at mid-chord length are controlled by a combination of M_{RA}, M_{TV} and M_{HR}. The sheeting angles are changed by moving the clew points along the curved tracks in green. The mid-twists alter manipulating the peak points along a similar track. As the mast section is rotated to a certain angle, the control points of the splines are also rotated to guarantee a smooth airfoil profile. The morphing of the red airfoils of Figure 3 is valid for foots and heads of main and jib, showing the ability of controlling locally the depth and sail twist.

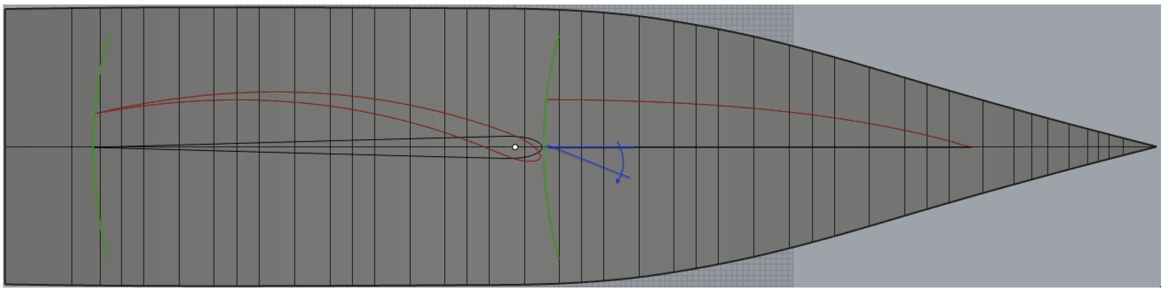

Figure 3. 2D-view of parametric sail section.

Figure 2 provides an overview of the parametric model structure displaying each trim control slider. The values of mid-twist and camber follow this convention: twist as geometrical angles of attack difference between foot and head, camber as depth percentage on chord length. The mid-twist follows a distribution close to linear and the main head is not designed to invert for any additional righting moment. The ranges with maximum and minimum values of mid-twist and camber are listed in Figure 2. For each trim, a number of sections are automatically generated and exported using a python script to be processed in the panel code as text files with coordinates of each sail.

3 NUMERICS

In the following section, the theoretical background of the employed numerical tools is provided.

3.1 Potential Theory Method BEM

The boundary element panel code “*pan*MARE” has been developed in-house by the Institute for Fluid Dynamics and Ship Theory at the Hamburg University of Technology (Institute of Fluid Dynamics and Ship Theory, 2020). Under the assumptions of incompressible, rotational, and inviscid potential airflow the fundamental equations for the potential Φ, the Laplace’s Equation and the Bernoulli´s Equation are reported in Equations 1 and 2.

$$\Delta\Phi = \nabla^2\Phi = 0 \tag{1}$$

$$p + \rho g z + \frac{1}{2}\rho\nabla\Phi^2 + \rho\frac{\partial\Phi}{\partial t} = k \tag{2}$$

With the linearity of the Laplace equation, Φ can be superposed in two independent solutions shown in Equation 3, one for external influences and one for induced potential by a lifting body in a flow field.

$$\Phi = \phi_e + \phi_i \tag{3}$$

The far-field condition shown in Equation 4 ensures that the aerodynamic influence of the lifting body vanishes towards infinity.

$$\lim_{|\mathbf{x}| \to \infty} \phi(\mathbf{x}) = \phi_\infty \tag{4}$$

With the assumptions that the lifting body is not traversed due to its boundaries and that the influence of the body disappears at infinity Green's identity can be used as a solution for the Laplace equation substituting the potential with sources and doublets on the boundary surfaces by means of wake surface S_{W} and body surface S_{B}, as shown by Figure 4. Considering the source strength defined as $\sigma = \frac{\partial \phi_i}{\partial n}$ and the doublet strength as $\mu = -\phi_i$, the induced velocity potential can be derived as in Equation 5, with n as normal vector and r as the distance between the point under consideration and the surface.

$$\phi_i = \frac{1}{4\pi} \int_{S_{\mathrm{B}}+S_{\mathrm{W}}} \left(\mu \frac{\partial}{\partial n} \left(\frac{1}{r} \right) \right) dS - \frac{1}{4\pi} \int_{S_{\mathrm{B}}} \left(\sigma \frac{1}{r} \right) dS = 0 \tag{5}$$

This Dirichlet formulation is based on the fact that the induced potential vanished inside the body assuring also that the induced potential is constant outside the fluid domain. To determine the unknown doublet and source strength, boundary conditions are required. Considering an additional boundary condition known as the Neumann boundary condition, the body should not be penetrated by the flow, meaning the velocity is set to zero on the normal body surface S_{B}:

$$\nabla(\phi_e + \phi_i) - \mathbf{u} \cdot \mathbf{n} = 0. \tag{6}$$

Furthermore, a wake trailing surface S_{W} is attached on the body trailing edge in order to prevent the flow from traveling between pressure and suction side: the linearized Kutta boundary condition ensures that the pressure jump between the two sides is set to 0 on the wake surface S_{W}. This linearization is valid as long as the flow is perpendicular to the trailing edge. If this is not the case, a non-linear formulation of the Kutta condition can be applied: a matrix is set up in which each entry contains the change in the pressure difference at a segment of the trailing edge divided by a specified change in the dipole strength on a wake panel. This matrix is then inverted and multiplied by the existing pressure difference to obtain the required change in dipole strength for a given small pressure difference.

A first-order panel method is used in *pan*MARE to calculate the flow field around a discretized body with quadrilateral or triangular elements. While the body surface S_{B} is discretized by a number of panels n_{B} with constant doublet σ and source μ strengths, the wake surfaces S_W, discretized with n_{W}, are only assigned with doublet strengths as the wake does not induce displacement. As common in most potential-based methods, each panel is assigned a collocation point in its center of gravity on the inside body. At the collocation points the boundary conditions are evaluated allowing a system of equations to be set up with doublet and source influence according to Katz and Plotkin (1991) shown in Equation 7 leading to the reformulation of the Dirichlet boundary condition in Equation 8.

$$A = \frac{1}{4\pi} \int_S \frac{\partial}{\partial n} \frac{1}{r} \, dS, \quad B = -\frac{1}{4\pi} \int_S \frac{1}{r} \, dS, \tag{7}$$

$$\sum_{j=1}^{n_{\mathrm{B}}}(B_{ij}\mu_{b,ij} + A_{ij}\sigma_{ij}) + \sum_{k=N_b+1}^{n_{\mathrm{B}}+n_{\mathrm{W}}} B_{ik}\mu_{w,ik} = 0 \tag{8}$$

The body panel source strengths σ_{ij} come from the Neumann condition and the doublet strengths on wake panels $\mu_{w,ij}$ are to be substituted using the Kutta condition. The remaining unknowns are the doublet strengths at the body panels $\mu_{b,ij}$ which are obtained from the solution of the linear equation system. The solving of the latter differs slightly for either steady or unsteady flow simulations. In steady flow, the wake doublet strength remains constant, facilitating potential evaluation using Neumann and Dirichlet boundary conditions. In unsteady cases, the body moves through the fluid while wake panels stay fixed until detachment leading to the insertion of new panels. Wake doublet strengths change for the first wake panels, with others maintaining previous values. This process parallels the steady case, allowing for direct body panel doublet strength calculation and determining wake panel strengths based on trailing edge differences using the Kutta condition.

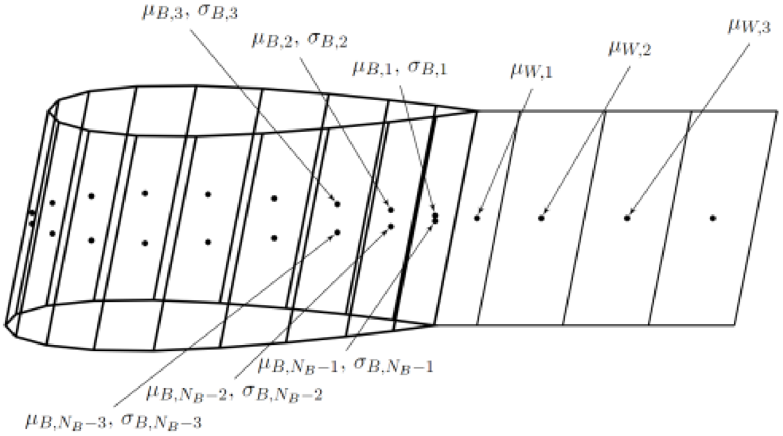

Figure 4. Hydrofoil discretization in *pan*MARE (Institute of Fluid Dynamics and Ship Theory, 2020).

Finally, the aerodynamic forces are evaluated from the pressure integration over all panels with the Bernoulli Equation (1). In quality of a potential-based method, *pan*MARE is not capable of accounting for flow separation while for viscous effects a semi-empirical correction is provided based on Schlichtling (1978). This involves adjusting the results of inviscid flow theory to account for the influence of viscosity, particularly near the boundary layer, regions in which viscous effects cannot be neglected, such as in high Reynolds number regimes.

3.2 Viscous Method RANS

To account for eventual viscous effects such as airflow separation to verify the results of the employed lower fidelity potential tool, viscous flow simulations are carried out using the commercially available numerical code Simcenter STAR-CCM+ version 18.04. With its finite volume approach, the tool solves the Reynolds-averaged Navier Stokes (RANS) equation simplifying the turbulent fluctuation by averaging them over time and neglecting the large-scale fluctuations. This helps save mesh resolution and computational effort and at the same time provides enough accuracy. Its fundamental equations are given in Equations 9 and 10: the mass continuity and the momentum conservation.

$$\frac{\partial \rho}{\partial t} + \nabla \cdot (\rho \mathbf{u}) = 0 \tag{9}$$

$$(\frac{\partial}{\partial t} + \mathbf{u} \cdot \nabla)(\rho \mathbf{u}) = -\nabla p + \nabla \cdot (\tau_m + \tau_t) + \mathbf{f} \tag{10}$$

In the above, $\mathbf{u}$ expresses the motion velocity vector, p is pressure, $\mathbf{f}$ for external forces and stress tensors τ_m and τ_t. To solve these equations, the shear stress tensor (SST) k-ω approach is used as a turbulence model. It uses a merging function in the boundary layer differentiating between near-the-wall regime and free flow. In order to be able to correctly model the shear forces and hence the velocity profile on the wall as a function of the non-dimensional wall distance y^+ a valid law is required. Considering the speed range, a two-layer structure, by means of a bottom layer and turbulent core layer, is used based on Schlichtling (1978). To model these within this project the center of the first cell near the wall is assumed to fall outside the bottom layer targeting a high y^+ approach, meaning less computational effort and less accuracy; for example in separation prediction which would require a low y^+ approach. The simulations for sails and hull are run steady and transient comparing results ensuring acceptable divergences.

3.3 STAR-CCM+ Sails & Hull Setup

Within this project, a selected sail trim and hull body was imported as an airtight CAD geometry in STAR-CCM+ with the highest tessellation density for isolated simulation of sails only and hull only. An appropriate domain size was set up after running different test sizes and consulting literature such as Birch-Tomlinson et al. (2022) and Gambacciani (2021). Several boundary conditions were defined: a pressure outlet is set at 350 meters from M_{RA} axis, a slip wall on the sails foots for endplating and velocity inlets at top, front, and sides respectively as 150 meters from the mast. The same setup has been used for the hull simulation elevating the hull above the slip wall for a specific ride height measured at transom of 0.8 meters allowing good bustle endplating. Guidelines for mesh size, and domain sizes were taken from Gambacciani (2021). Sails and hull are defined as no-slip walls with a boundary layer mesh. Several iterations were run to establish the correct size of the first cell on the wall ensuring the y^+ to fall between 30 and 300. In all simulations, the segregated flow solver is used for velocity and pressure, the flow regime is turbulent in the boundary layer where the k-ω-SST model was used. For eventual regime transitions from laminar to turbulent, the gamma model was also selected. The mesh consists of approx 10 million cells for the main+jib trim case and 5 million cells for hull only case, used as benchmark simulation for the respective *pan*MARE case. Volumetric and surface mesh refinement were arranged for the wake shedding and the thin jib leading and trailing edges. Grids for sails and hull simulations are displayed in Figures 5 and 6 below.

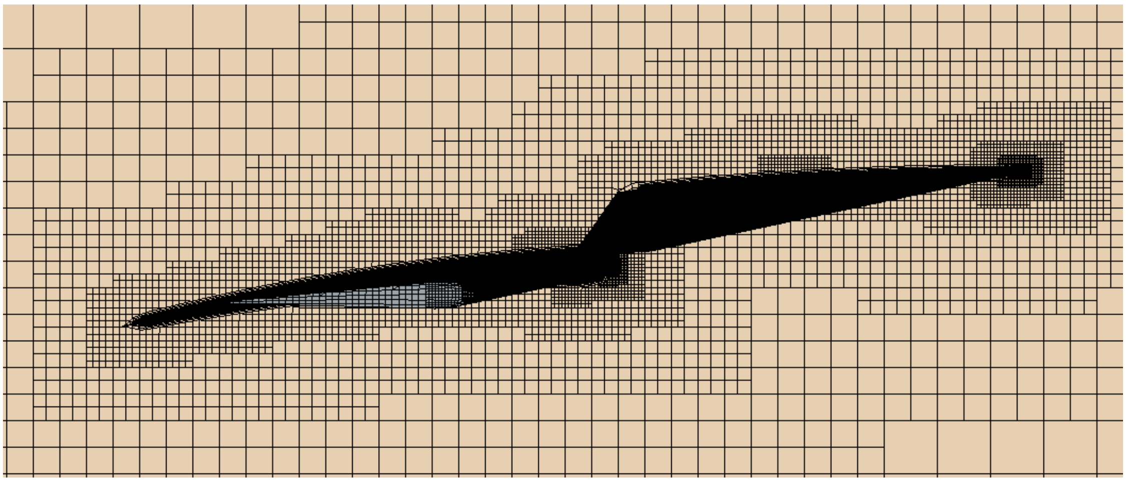

Figure 5. Top view sails mesh in STAR-CCM+.

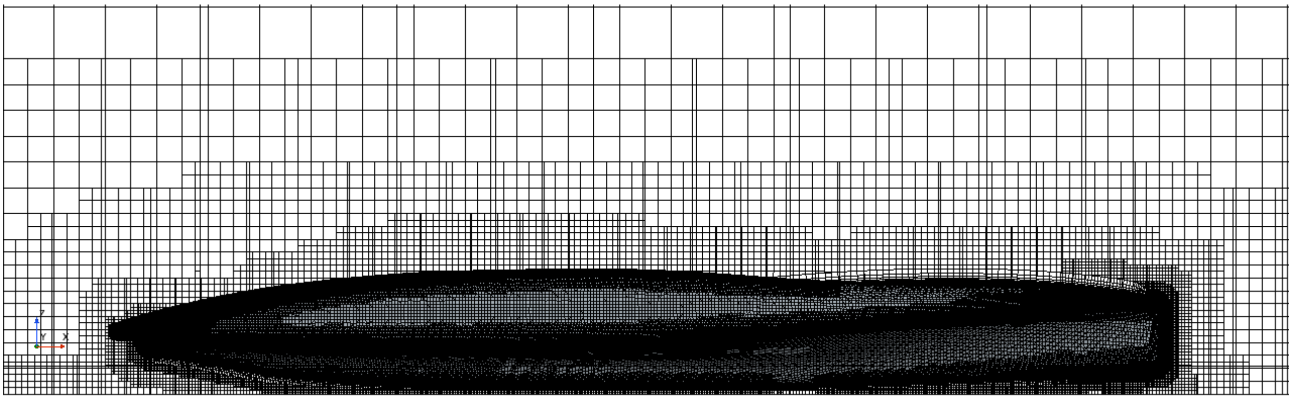

Figure 6. Side view hull mesh in STAR-CCM+.

3.4 *pan*MARE Sails Setup

The prediction uncertainties of *pan*MARE for three-dimensional lifting bodies with geometries similar to the AC75 double-skin main in terms of thickness, have already been assessed as the BEM tool has been validated with experiments and higher fidelity predictions (Schmitt et al., 2018) (Goettsche, 2020). As body and wake discretization plays a fundamental role in force prediction, grid convergence studies were carried out varying the time steps t for the distribution of body and wake panels on each sail. For the double-skin main, the chord panel spacing at the leading edge has been refined for better flow capturing around mast with longer panels towards the trailing edge matching the wake sheet panels while keeping a rather simple spacing in span. This grid is displayed in Figure 7. For the wake several runs were executed targeting a reasonable wake length and grid size. The wake deformation of each sail was analyzed, adjusting, when needed, the desingularization factor and hence the finite width ensuring no singularity points. For two sails simulation using the parametric trims, much attention has been paid to monitoring the eventuality of jib wake shedding onto the main as no correction for this eventuality has been implemented in the model yet. To fulfill near to identical pressure distribution on suction and pressure sides of the trailing edge the non-linear Kutta condition was used. In the initial absence of the hull body, one option would have been to place the mirror plane at the waterplane with a gap for the sails. However within this setup, the sails are end-plated on the deck with a symmetry plane located at a specific height above a theoretical waterline considering usual foiling ride heights. For the sail simulations, a logarithmic A_{WS} gradient over vertical height has been used with a reference height of 10 meters. With a semi-empirical frictional correction according to Schlichtling (1978), it is possible to increase the total drag by approximately 5%. All simulations have been run steady for less time-consuming results. For each simulation, 20 iterations were computed until the coefficient reached convergence criteria of 0.5% deltas between the last iteration steps.

To generate thin sails in *pan*MARE, representing the AC75 jib, a list of coordinates is imported to create sections along several span sections. Then a thickness value normal to the camber line has been assigned to each section targeting the minimum possible value to avoid numerical issues. After several tests gradually decreasing the thickness value, the smallest possible value of 3 mm was achieved beyond which the software encountered convergence errors. To compute the velocity distribution on neighboring panels, the first-order BEM code uses the velocity gradients. The accuracy of the passed information depends on the gradients and hence this can be done only for neighboring panels that are not separated by a sharp edge. For example for the sharp jib leading edge, the code was modified converting the edge into a knuckle ensuring that the gradients are not computed there avoiding discontinuities in the velocity distribution. This issue could have been solved by implementing a leading-edge vortex correction. For the trailing edge, this problem does not occur as the Kutta condition must be valid. A further important aspect when modeling thin lifting surfaces is the symmetry of the grid on the pressure and suction sides to avoid any incorrect interference between doublets.

3.5 *pan*MARE Hull Setup

As the hull body plays a fundamental role in the overall aerodynamic package of an AC75, also confirmed in Gambacciani (2021), it is firstly imported in *pan*MARE for a hull-only test simulation. The fine mesh consists of 1000 panels to allow flexibility in edge specifications for wake shedding and to preserve the hull curvatures. The hull simulation in *pan*MARE is tuned based on the discussed benchmark finite volume simulation providing detailed solutions for each part of the hull body. Similar as for the jib, on discrete sharp edges the gradients calculations were suppressed in the code, for example for the bow edge and transom. On the latter, all panels were excluded for gradient computation as the physics of the dead air cannot be modeled in the potential-based flow solver. A test simulation was set up on a symmetrical cylinder to test vortices placement and their initialization as this method was never applied in *pan*MARE before, showing promising results. On the hull, several settings were tested de- or activating wake deformation while adjusting each desingularization factor. A symmetry plane has been defined depending on targeted ride heights to display the presence of a water surface. For combined hull and sails simulations, the grid required some modifications with matching panel sizes on the deck and sail foots to avoid any peaks resulting from numerical interference between doublets. The combined grid is displayed below in Figure 7.

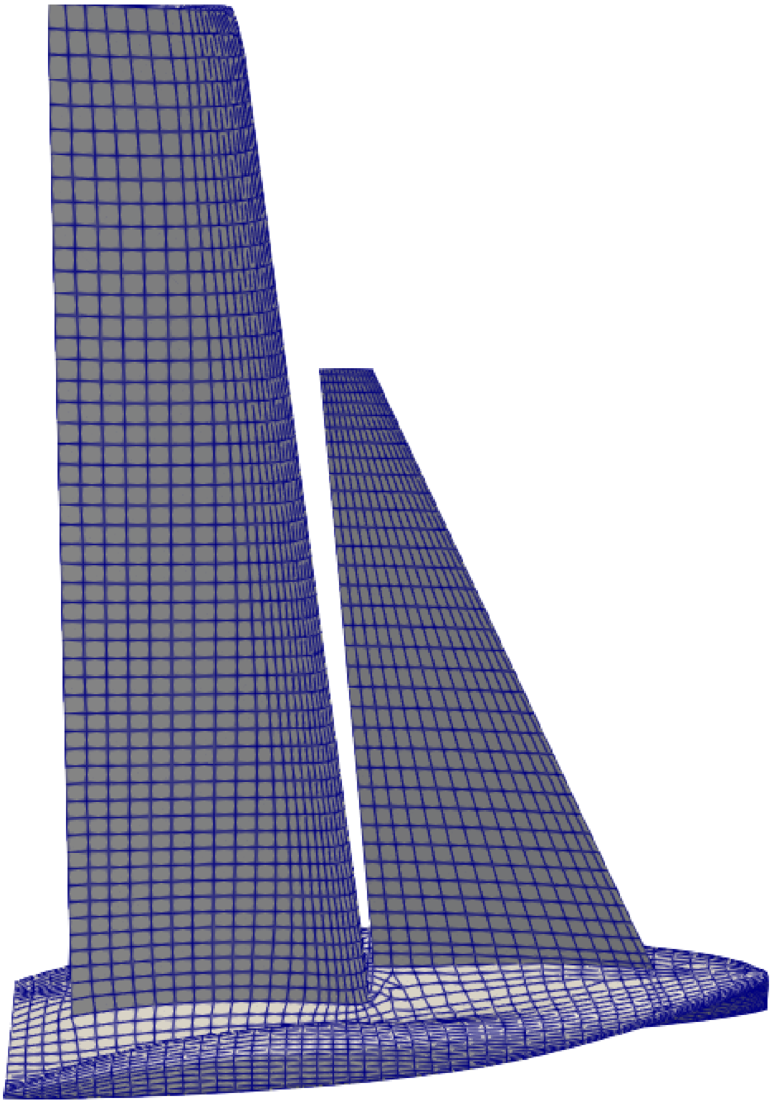

Figure 7. Combined sails & hull grid in *pan*MARE.

4 HULL IMPLEMENTATION

To quantify the modeling error beforehand, the ability of *pan*MARE to model flow around a blunt body is tested on an AC75 hull before running a combined hull and sails simulation. The geometry used for the AC75 hull in *pan*MARE is displayed in Figure 8 with defined characteristic hull edges.

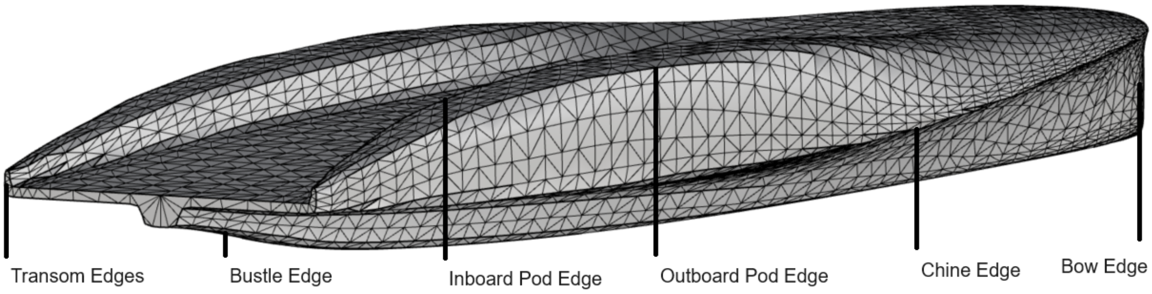

Figure 8. Characteristic edges of the AC75 hull.

As discussed within the setup, a finite volume simulation was run in STAR-CCM+ for the drawn AC75 hull body under upwind sailing conditions: A_{WA} of 14.64 degrees and A_{WS} of 20.98 m s^{-1}. An accurate analysis of airflow behavior in terms of flow separation, flow direction, and vortex shedding was undertaken within the STAR-CCM+ simulation. Several scenes were set up to monitor wall shear stress components, constrained streamlines, and velocity vorticity using Q-criterion, for example displayed in Figure 9. Considering that the hull is being sailed on starboard tack, shedding vortices can be noted on the inboard windward pod edge, on the outboard leeward pod edge, on the bustle and transom edges. Considering the hull geometry and limitations of *pan*MARE, certain shedding vortices could not be initiated on edges where they would stream onto other lifting panels as no correction is implemented in the software yet. This is the case for the vortex shedding from the sharp bow and inboard windward pod edge, where gradient computation suppression defining these as knuckles was the only option. Figure 9 displays front, aft and leeward views.

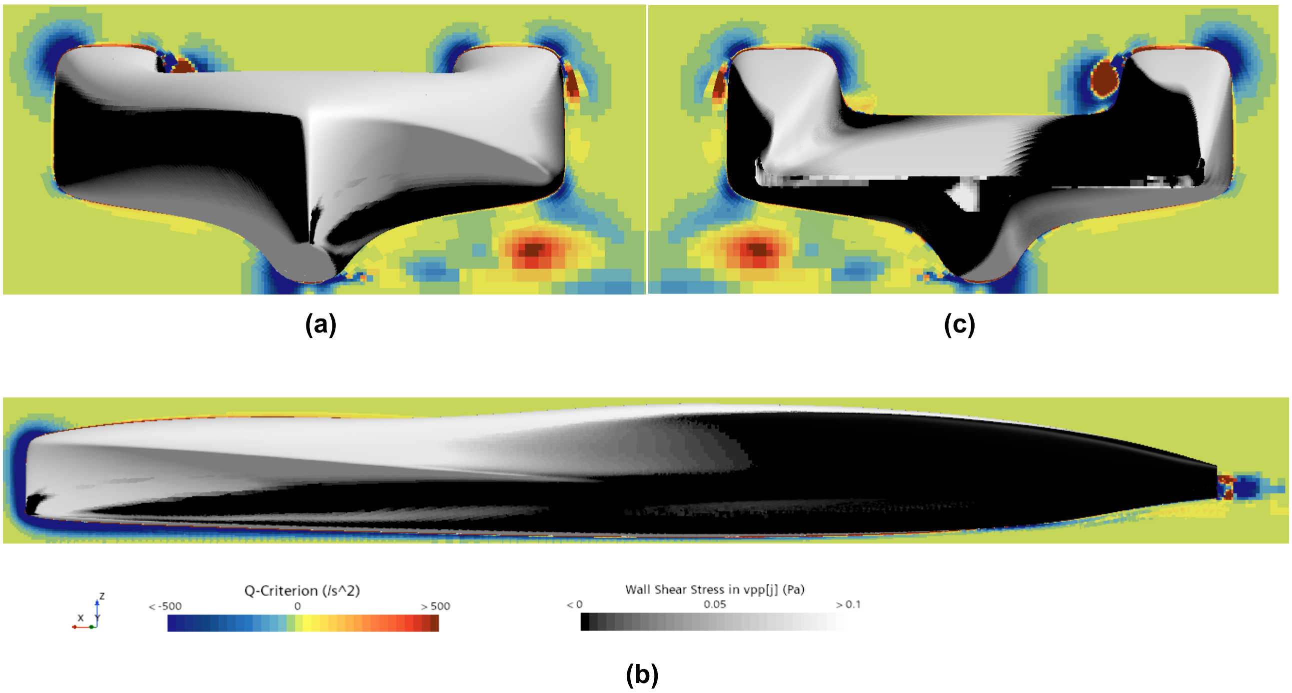

(a)

(c)

(b)

Figure 9. Q-criterion on plane and wall shear stress on hull: $A_{\mathrm{WA}} = 14.64°$ and $A_{\mathrm{WS}} = 20.98$ m s^{-1}.

Particular attention was drawn to the largest C_P divergences between STAR-CCM+ (a)(d) and *pan*MARE to identify regions where *pan*MARE would show the highest pressure gradients, displayed in Figure 10. These diverge significantly between the two methods, especially due to the flow solutions on certain hull areas such as the bow, transom, bustle, and pod edges. Based on these learnings, discrete edge lists were selected in the *pan*MARE mesh and used either for gradient computation suppression on sharp edges or for initialization of wake-shedding panels considering their starting positions and development downstream. Figure 10 shows a comparison for C_P between the STAR-CCM+ and two *pan*MARE: without (b)(e) and with (c)(f) knuckles and un-deformed wakes.

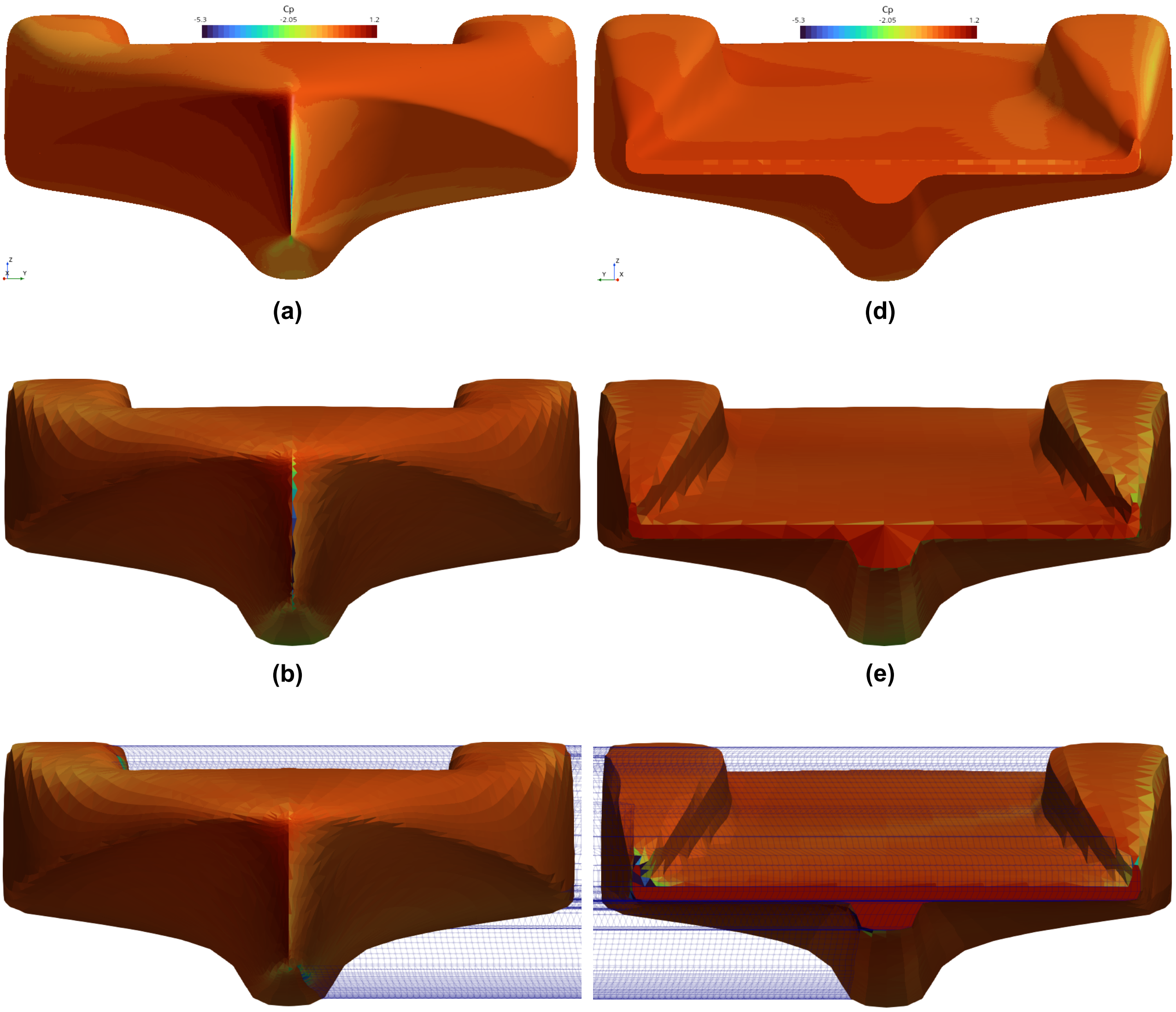

(a) (d)

(b) (e)

(c) (f)

Figure 10. Comparison of C_P distributions between STAR-CCM+ (a)(d) and *pan*MARE (b)(e)(c)(f).

As it can be seen, *pan*MARE is not able to entirely reproduce the pressure distribution of the sharp bow, even defining a knuckle there. On edges that share wake panels such as leeward bottom transom and aft chine, the wake needed to be shortened causing higher pressure gradients on the ends. However, comparing the first and third row C_Ps, it can be said that the *pan*MARE version with knuckles and wakes diverges less compared to the one without. This is also confirmed by the trends of the resulting forces. The divergences can also be explained by the rather simple frictional correction, no turbulent flow model, and different mesh sizes. Nonetheless, for this project's aim, this approach was used to include the hull in the sail simulations to study its direct effect on sails.

5 SAIL TEST-CASES

Before applying the *pan*MARE setup on the AC75 sails, selected test cases from the literature were reproduced in *pan*MARE to establish uncertainties on the applicability of the panel code for thin sails.

5.1 Thin Sails

Masuyama et al. (2009) presented a database of full-scale three-dimensional sail shapes along with their coordinates and respective aerodynamic coefficients measured by a sail dynamometer mounted on the 'Fujin' yacht for upwind conditions referring to the International Measurement System (IMS). Out of several conditions, test-case '98110105' with a thin main and a thin jib in A_{WS} 8.6 m s^{-1} has been selected and reproduced in *pan*MARE based on the lowest A_{WA}, considering typical A_{WA}s of an AC75. The provided sail coordinates (Masuyama et al., 2009) have been imported to model the sails. Table 1 presents a comparison of *pan*MAREs predicted aerodynamic lift, drag, drive, and side force coefficients to the referenced experiment and to an additional source (Deperrois, 2021). In the latter, the authors have used the same 'Fujin' experiment to establish uncertainties on their developed VLM code itself as reported in Deperrois (2021). In a VLM, the lifting body and its surrounding flow field are represented by a lattice of discrete vortices with collocation points placed at the three-quarter-chord position while the shedding wake stream is modeled with a vortex particle wake method (Katz and Plotkin, 1991). Even if in theory the experiment has a higher fidelity, some uncertainties must be kept in mind: the consistency of measured strength, direction and gradient of the wind, correct reading of flying shape coordinates, and calibration of measurement tools. However, with an A_{WA} of 20.5°, flow separation might occur, which should be captured by the measurement and not by the employed potential-based tools. In addition, the referenced experiment literature does not provide an exact wind gradient over height and its reference coordinate system point. The deltas can also be linked to different discretizations. However, analyzing the coefficients divergences, the *pan*MARE thin sail predictions for two sail surfaces show an acceptable agreement.

Table 1. Comparison of aerodynamic force coefficients: $A_{\text{WA}} = 20.5°$ and $A_{\text{WS}} = 8.6$ m s^{-1}.

	C_{L}[-]	C_{D}[-]	C_{FX}[-]	C_{FY}[-]
*pan*MARE	1.31	0.19	0.28	1.29
Deperrois (2021)	1.19	0.12	-0.36	1.14
Masuyama et al. (2009)	1.15	0.20	0.22	1.15

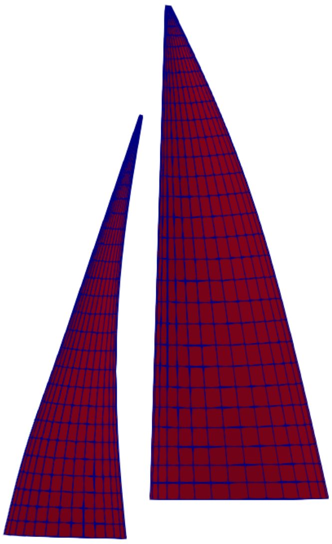

Figure 11. *pan*MAREs discretization of 'Fujin' sail plan.

5.2 AC75 Mainsail

Now that it has been verified that *pan*MARE has the ability to handle very thin and near-placed lifting bodies with acceptable accuracy, another test-case analysis can be carried out for the developed AC75 mainsail parametric model and indirect accuracy proof of the used flow solver. In Smith and Wright (2021) and Smith and Wright (2022) studies were presented on how the deformation under load of an AC75 mast and double-skin main affects its aerodynamic properties. As flow solvers, RANS-based and potential-based inviscid Euler methods have been employed while the structure is simulated using a geometrically nonlinear model for an elastic membrane that maintains a tension field within the sailcloth. Within these investigations rigid and elastic simulations were performed over a range of sails A_{OA}, in this case, identical to A_{WA}. The geometrical properties for this specific main trim are: mast raked at 5 degrees, M_{RA} 10 degrees, foot camber 2%, and head twist 5 degrees. This main trim has been mirrored in the developed parametric model and run in *pan*MARE. All simulations are arranged for an A_{WS} of 20 m s^{-1} without any vertical shear and without a symmetry plane at the foot for endplating. The resulting *pan*MARE predictions are displayed in Figure 12 along with all the rigid main computations conducted within the referenced solvers. The drag and lift coefficients predicted by *pan*MARE follow a similar trend of the Euler simulations which are not provided for 14 degrees A_{WA} as airflow separation prevailed according to Smith and Wright (2022). Compared to RANS, the drag force is quite small as for this comparison no friction is activated in panMARE, and separation is not accounted for. The lift and drag coefficients predicted by RANS diverge from the potential-based method results with increasing A_{WA} due to friction and perhaps separation effects. Considering the convention for A_{OA} and hence A_{WA} used by the author, it must be kept in mind that the main is not expected to be trimmed this way in reality as the angle difference between M_{RA} and A_{WA} rarely exceeds 3 degrees. In addition, these simulations are run the for mainsail only meaning that for the two-sail configuration, the incoming flow is diverted by the jib and the A_{WA} on the main is decreased also while trimming the M_{RA} and adjusting the traveler M_{TV} with the twist profile of the main. Assuming the sail geometries are entirely identical, this comparison also reveals some correlation for the accuracy of the developed AC75 parametric sail model as according to Figure 12 the results follow a similar trend.

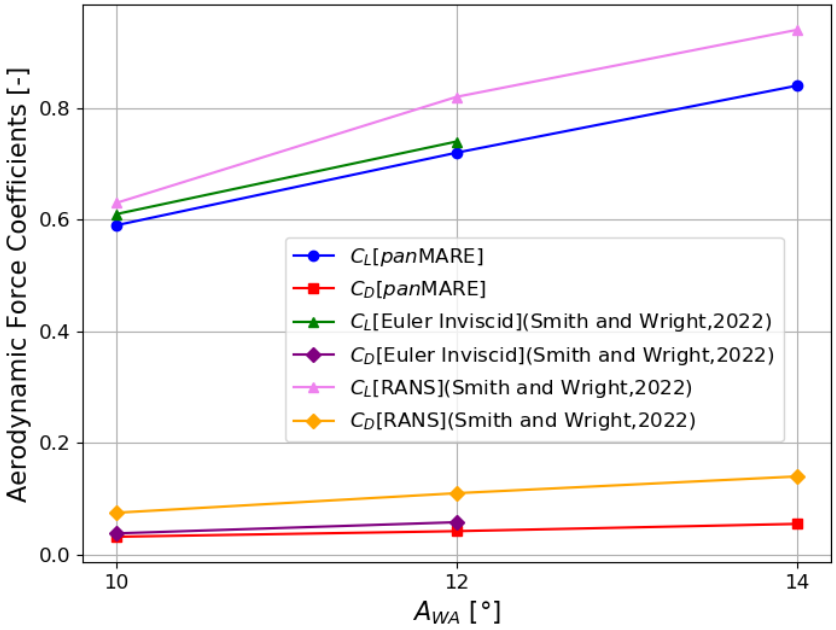

Figure 12. Comparison of aerodynamic force coefficients.

5.3 AC75 Sails

Acknowledging the two test cases above, a third test case is conducted for the entire AC75 sail plan. An example sail trim has been generated, imported, and computed in *pan*MARE. The resulting coefficient of pressure C_{P} distribution on main and jib sails is shown in Figure 13 revealing a quite loaded trim in an A_{WA} of 17.5 degrees and A_{WS} of 18 m s^{-1} (35 kn). It can be seen that the jib wake streams around the leeward main skin and hence influences its flow entry angle decreasing its suction pressure peak. Additionally, the tip and foot vortices are shown shedding downstream from each sail. The vortices have been deformed adjusting the desingularization factor considering the fully end-plated sails at deck via symmetry plane.

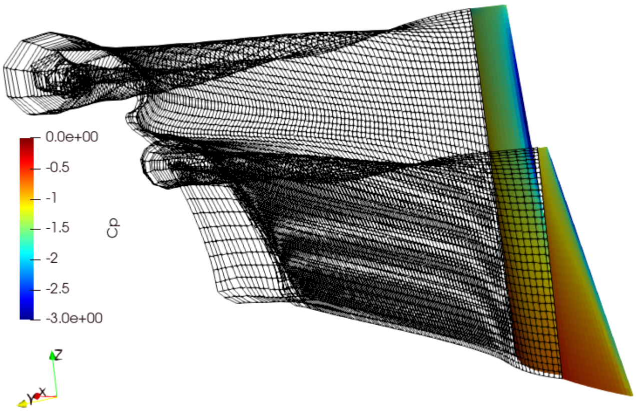

Figure 13. Wake and coefficient of pressure distribution: $A_{\text{WA}} = 17.5°$ and $A_{\text{WS}} = 18$ m s^{-1}.

As the convergence criteria were met for the most extreme trims ensuring a grid able to handle all shapes, a broader trim matrix was run for a further comparison. The task is to show the difference in achievable drive and side force coefficients between the *pan*MARE model and a semi-empirical IMS formulation (Tannenberg et al., 2023) for the same sail dimensions. This comparison was done in order to provide feedback on force magnitudes as no specific literature could be found on this topic. The matrix was run for an upwind, A_{WA} 11°, and a downwind, A_{WA} 15°, condition. Out of all computed data points, those with identical IMS C_{FY} and largest C_{FX} have been reported in Table 2. For the upwind condition, flatter sail trims and more de-powering twist while, for the downwind condition, more depth and less twist prevailed. The ratios between IMS and *pan*MARE drive force coefficients are 1.4 for upwind and 1.44 for downwind. These are both higher than the empirical coefficient 1.3 used by Tannenberg et al. (2023) increasing the drive force by 30% accounting for the higher efficiency of the AC75 rig compared to a classic IMS rig. These differences show that for those conditions there is potential in extracting more drive from the sail plan. This can be perhaps explained by the rotating mast and the double-skin main efficiency along with the fully end-plated sails. However one must keep into account, the neglection of flow-separation. Particularly the ability to generate higher drive forces has been one of the major driving factors for this project hence being able to increase the accuracy of previously developed VPP. However, adding 30% more drive force to the model can lead to inaccuracies neglecting how more drive force affects the other coefficients.

Table 2. Comparison of aerodynamic force coefficients.

	C_{FX}[-]	C_{FY}[-]	C_{FX}[-]	C_{FY}[-]
*pan*MARE	0.14	0.94	0.23	1.13
Tannenberg et al. (2023)	0.10	0.95	0.16	1.14
A_{WA}	11°	11°	15°	15°

To confirm whether there is a real possible gain, the force and moment coefficients are to be implemented in surrogate response surfaces for the VPP, which undeniably serves as the ultimate arbiter for performance balancing force and moments in all six degrees of freedom by optimizing boat speed while adjusting the trim parameters.

6 AC75 VPP

For the VPP model, the software tool 'FS-Equilibrium' (Hochkirch, 2018) was used as it offers a validated modular workbench. The tool has been successfully used for high-performance hydro-foiling yachts in a number of projects such as for the C-Class Catamaran Groupama (Paulin et al., 2015), the AC50 (Hansen et al., 2019) and the QFX Lake Racer (Melis et al., 2022). The program estimates the performance of a sailing yacht given certain boat model and environmental data. Two algorithms are employed in different loops: the first one searches the equilibrium condition by adjusting the state variables, while the second is employed in an outer optimization loop searching for maximum speed changing the defined set of trim values. All the forces acting on the sailing yacht are modeled in so-called 'force modules', displayed by the GUI in Figure 14. A stationary VPP model for the AC75 was initially developed by Tannenberg et al. (2023) presenting its detailed setup as per below.

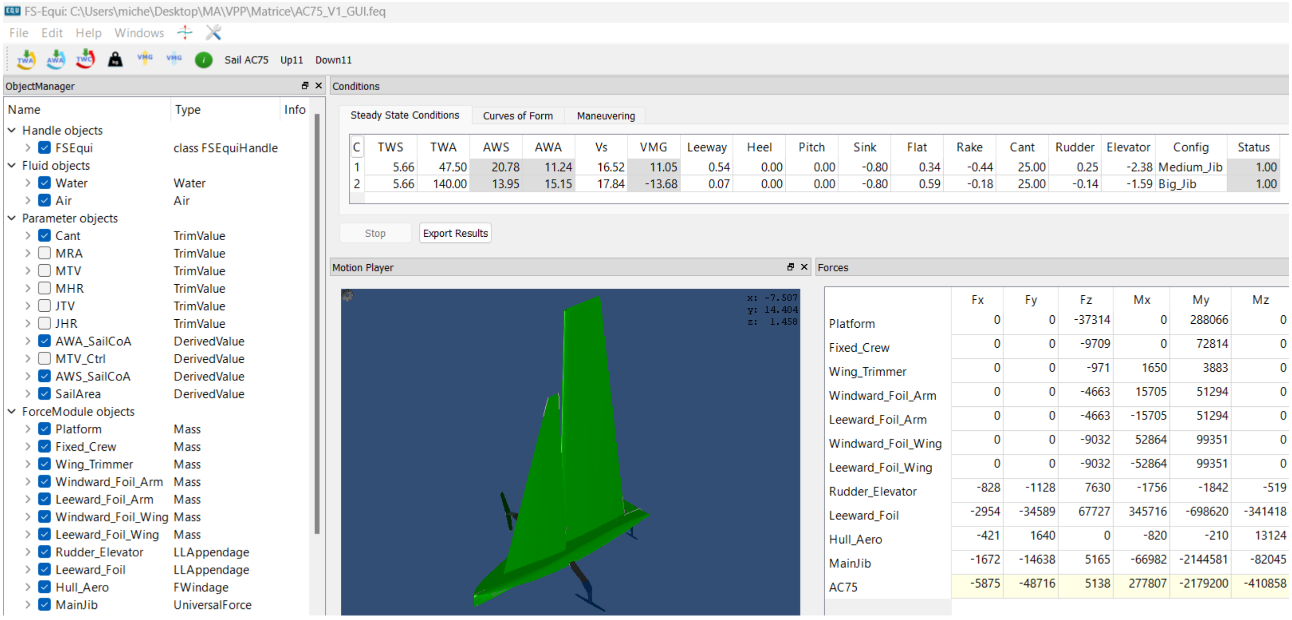

Name	Type	Info
Handle objects		
☑ FSEqui	class FSEquiHandle	
Fluid objects		
☑ Water	Water	
☑ Air	Air	
Parameter objects		
☑ Cant	TrimValue	
☐ MRA	TrimValue	
☐ MTV	TrimValue	
☐ MHR	TrimValue	
☐ JTV	TrimValue	
☐ JHR	TrimValue	
☑ AWA_SailCoA	DerivedValue	
☐ MTV_Ctrl	DerivedValue	
☑ AWS_SailCoA	DerivedValue	
☑ SailArea	DerivedValue	
ForceModule objects		
☑ Platform	Mass	
☑ Fixed_Crew	Mass	
☑ Wing_Trimmer	Mass	
☑ Windward_Foil_Arm	Mass	
☑ Leeward_Foil_Arm	Mass	
☑ Windward_Foil_Wing	Mass	
☑ Leeward_Foil_Wing	Mass	
☑ Rudder_Elevator	LLAppendage	
☑ Leeward_Foil	LLAppendage	
☑ Hull_Aero	FWindage	
☑ MainJib	UniversalForce	

C	TWS	TWA	AWS	AWA	Vs	VMG	Leeway	Heel	Pitch	Sink	Flat	Rake	Cant	Rudder	Elevator	Config	Status
1	5.66	47.50	20.78	11.24	16.52	11.05	0.54	0.00	0.00	-0.80	0.34	-0.44	25.00	0.25	-2.38	Medium_Jib	1.00
2	5.66	140.00	13.95	15.15	17.84	-13.68	0.07	0.00	0.00	-0.80	0.59	-0.18	25.00	-0.14	-1.59	Big_Jib	1.00

	Fx	Fy	Fz	Mx	My	Mz
Platform	0	0	-37314	0	288066	0
Fixed_Crew	0	0	-9709	0	72814	0
Wing_Trimmer	0	0	-971	1650	3883	0
Windward_Foil_Arm	0	0	-4663	15705	51294	0
Leeward_Foil_Arm	0	0	-4663	-15705	51294	0
Windward_Foil_Wing	0	0	-9032	52864	99351	0
Leeward_Foil_Wing	0	0	-9032	-52864	99351	0
Rudder_Elevator	-828	-1128	7630	-1756	-1842	-519
Leeward_Foil	-2954	-34589	67727	345716	-698620	-341418
Hull_Aero	-421	1640	0	-820	-210	13124
MainJib	-1672	-14638	5165	-66982	-2144581	-82045
AC75	-5875	-48716	5138	277807	-2179200	-410858

Figure 14. FS-equilibrium GUI for the AC75 VPP model.

6.1 Solver Setup

To mirror how the AC75 is sailed in reality the solver was set up in the following way (Tannenberg et al., 2023): boat speed V_{S} balances the drive force in the x-direction, the leeway angle λ balances the side force in the y-direction, the flap angle δ_f balances the vertical force in the z-direction, the rudder angle δ_r balances the yawing moment. The additionally defined variable for elevator angle δ_e balances the pitching moment while another, called flat parameter τ, balances the heeling moment. In the model, the ride height d_{Z}, cant angle γ, heel angle ϕ, and pitch angle θ are held constant to specific values (Tannenberg et al., 2023). The flat τ serves as sheet power, de- or increasing the C_{L} and so the induced drag, the frictional profile drag depends on C_{L}. These coefficients are based on default response functions according to IMS rules in function of the A_{WA}. The use of the IMS coefficients and one-only sail trim parameter for an entire AC75 sail plan introduces some inaccuracies that are targeted in this project. With the newly defined five sail trim sliders, the sail trimming acquires control ability and hence some changes in boat performance can be expected. The above-introduced setup was modified so that the main traveler M_{TV} is used to balance the heeling moment. Other sail trim controls such as M_{RA}, M_{HR}, J_{TV} and J_{HR} can be optimized as trim values to maximize boat speed and be adjusted manually to help the VPP find an initial equilibrium condition.

6.2 Aerodynamic Matrix

After running various tests, a total of 2250 points were computed in *pan*MARE for different A_{WA}: 9, 12, 15, and 18 degrees. The computational time of these lies between 8-9 hours on a 12-core machine. Approximately 80 seconds were required by *pan*MARE per simulation to reach convergence after 20 iterations. To generate response surfaces within FS-Equilibrium, a 'Universal Force Module' (Hochkirch, 2018) was used, providing a broad choice of interpolation functions. Of the latter, several were considered for the correct fitting of the matrix leading to the selection of a sequential spline function. Sequential splines use piecewise polynomials, or splines, to approximate more complex functions by adding knots or adjusting the splines depending on the complexity of the data. All points are used to train the model. By being a potential-based code, the first-order panel code outputs linear lift and parabolic drag, therefore the response surfaces should be able to capture this. This results in a minimum of 3 points per sail trim parameter. For this reason, where possible, 3-4 stations were set up to detect outliers considering this a good compromise for all trim controls. For M_{RA} less stations were used considering its realistic operational range. The fitting error, expressed in percentage between fitted value and actual value, is computed on the actual data points and shown in green for each point in the Figures below indicating 0% error using the sequential spline function. As this study was conducted without a clear required quantity and distribution of data points necessary to accurately capture the force and moments variation of each trim parameter and how these affect the boat's performance, initial sensitivity checks were run to establish an approximate amount of required points. This was done to avoid expensive and large aerodynamic data matrices. At first, large coarse matrices with wider point variations with a rather poor linear fit were computed, and imported into the VPP to search for a possible equilibrium condition. Several iterations led to select a design trim space. The code output consists of several text files containing the status of each sail trim parameter for each coefficient: C_{FX}, C_{FX}, C_{FY}, C_{MX}, C_{MZ} and C_{MZ}. These are computed using a constant A_{WS} of 20 m s^{-1} after running some tests showing a weak dependence from it. This can be reasoned by the weak impact of the empirical frictional correction on each panel forces, approximately 5 % of total drag. These are normalized in the code with dynamic pressure and scaled again in the same way within the force module. As the moment coefficients are firstly computed in the *pan*MARE origin, these are then transformed to the VPP origin. In the model, the wind pressure is from starboard tack and the coordinate system convention is: positive x-direction pointing forward, positive y-direction pointing to port, and positive z-direction upwards. Plausibility checks have been carried out for force and moment output of an example response point crosschecking it with the *pan*MARE code. The variations and dependencies of each trim control and coefficients depend highly on how the geometries are morphed in CAD and an FSI solver would definitely differ in results. For example, FSI would show that changing the M_{RA} would affect the mast bending, and thus the sails camber and twist distributions.

7 RESULTS

This section is devoted to the output of *pan*MARE as response surfaces and how these influence two selected sailing conditions of the VPP with a T_{WS} of 5.66 m s^{-1} (11 kn). Considering the sail trim controls and apparent wind angles in a six degrees of freedom simulation, a few response surfaces were selected for further discussion. A comparison is provided between the equilibrium condition computed with the IMS sail coefficient and the one of *pan*MARE for one upwind and one downwind sailing case where the divergencies are discussed. Furthermore, the performance of a specific sail trim is validated with a higher fidelity volume method and comparisons are shown for hull influence on sail performance employing tools with different fidelity degrees.

7.1 Response Surfaces

Figure 15 reveals the variation of C_{FX} as a function of each different sail trim control. According to Figure 15a, the drive force increases significantly with A_{WA} and slightly with M_{RA}. In principle, a larger angle difference between M_{RA} and A_{WA} results in more main depth. As shown by 15b the drive force increases with M_{TV} hence moving the travelers towards amidship. Figure 15c suggests also that C_{FX} grows with M_{HR} because of the camber induced in the upper sections. For the jib trim controls, Figures 15d reveals a slight change in C_{FX} sheeting in the J_{TV} as, due to its geometry morphing, the sail loses depth and gets flatter. Depowering the jib head causes a slight reduction of drive force by changing the J_{HR} and hence increasing the twist.

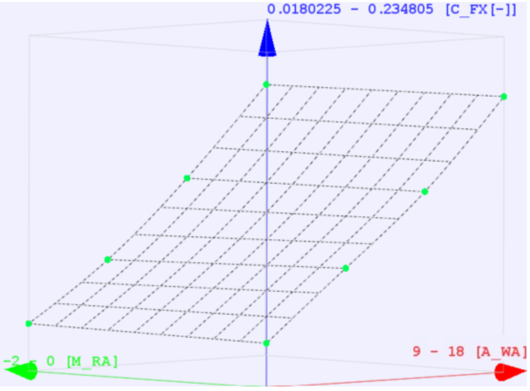

(a) C_{FX} in function of M_{RA} and A_{WA}

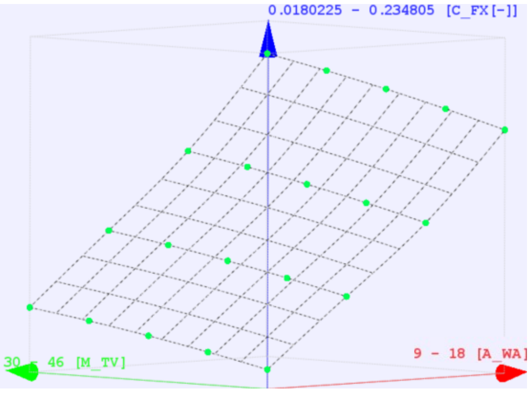

(b) C_{FX} in function of M_{TV} and A_{WA}

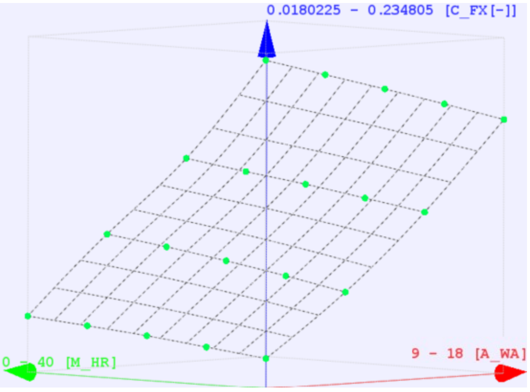

(c) C_{FX} in function of M_{HR} and A_{WA}

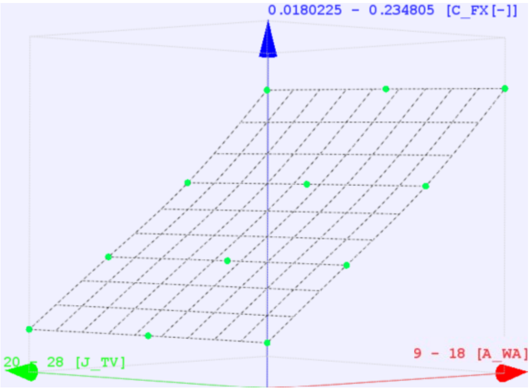

(d) C_{FX} in function of J_{TV} and A_{WA}

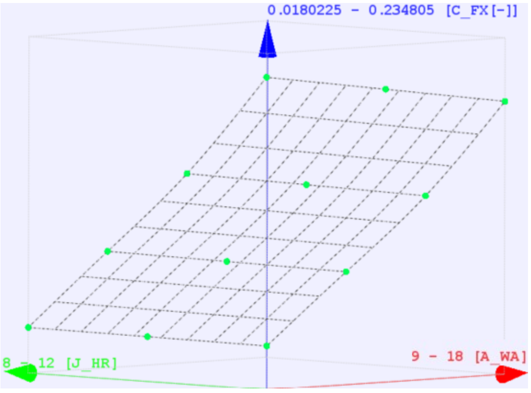

(e) C_{FX} in function of J_{HR} and A_{WA}

Figure 15. Response surfaces of C_{FX} for main (left) and jib (right) trim controls over A_{WA}.

Figure 16 reports the variation of the side force coefficient as a function of each different main and jib trim controls and A_{WA}. As one would expect, the C_{FY} grows significantly with A_{WA}. According to 16a the side force increases slightly with M_{RA} considering the induced depth with larger values. The total side force increases with sheeting in the M_{TV} and J_{TV} as shown by 16b and 16d. Reducing the A_{OA} by means of increasing the twist in the upper section of each sail, hence by reducing the values of M_{HR} and J_{HR} decreases the side force, which is plausible. The M_{HR} trend influences also the heeling moment in a similar way, as to be seen in Figure 17.

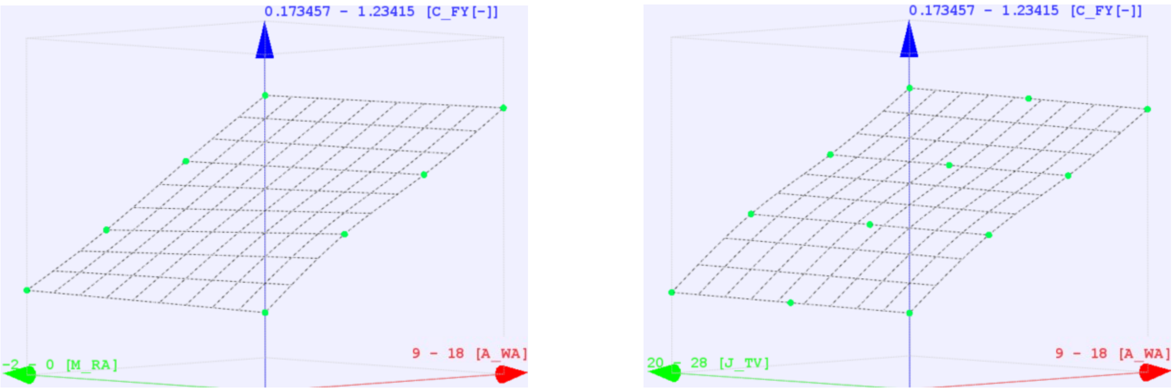

(a) C_{FY} in function of M_{RA} and A_{WA}

(d) C_{FY} in function of J_{TV} and A_{WA}

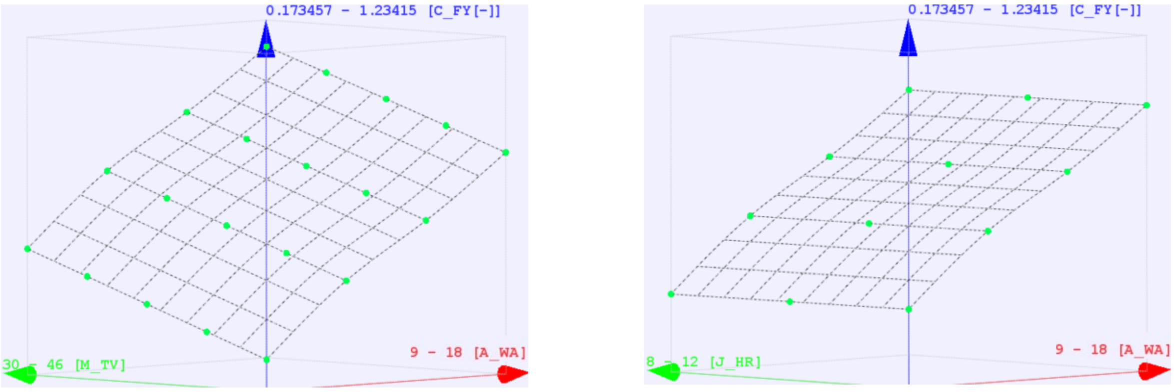

(b) C_{FY} in function of M_{TV} and A_{WA}

(e) C_{FY} in function of J_{HR} and A_{WA}

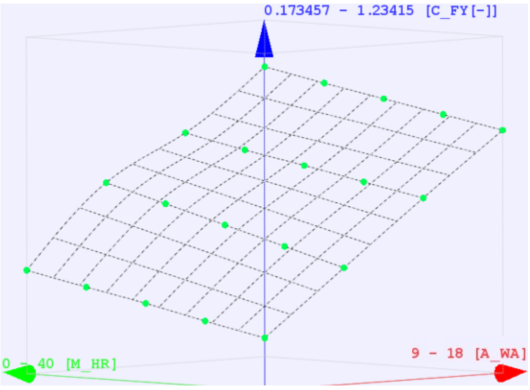

(c) C_{FY} in function of M_{HR} and A_{WA}

Figure 16. Response surfaces of C_{FY} for main (left) and jib (right) trim controls over A_{WA}.

Figure 17 reveals the variation of C_{MX} as a function of each different sail trim control. Negative values are shown in the coordinate system, increasing absolute values from top to bottom. According to Figure 17, the increment on heeling moment with increasing M_{RA} is quite weak while it increases for larger A_{WA}s. This complies with the trends observed for the side force coefficients. Also, the heeling moment increases linearly with changes of M_{TV} which is expected to increase COE´s height. On the other hand, less side force and a reduction of the COE´s height, result in a decrease of heeling moment coefficient C_{MX}. On the jib controls, the jib traveler J_{TV} increases the sheeting angle and hence the heeling moment while J_{HR} opens up the sail and decreases slightly the heeling moment.

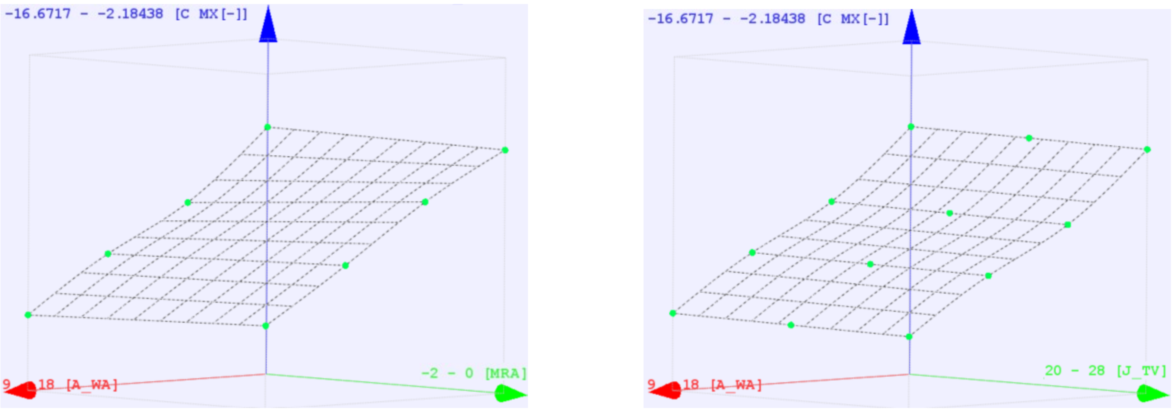

(a) C_{MX} in function of M_{RA} and A_{WA}

(d) C_{MX} in function of J_{TV} and A_{WA}

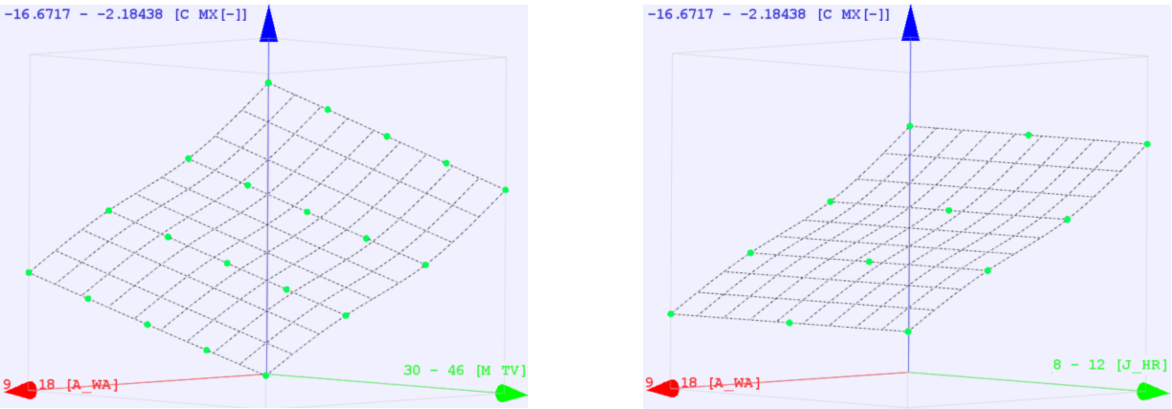

(b) C_{MX} in function of M_{TV} and A_{WA}

(e) C_{MX} in function of J_{HR} and A_{WA}

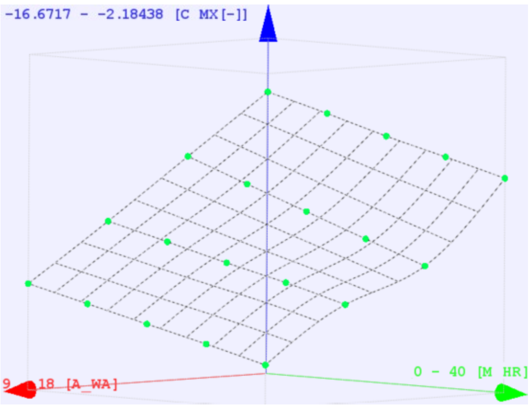

(c) C_{MX} in function of M_{HR} and A_{WA}

Figure 17. Response surfaces of C_{MX} for main (left) and jib (right) trim controls over A_{WA}.

The heeling moment variation in a specific sailing condition is balanced by the adjustment of the main traveler M_{TV}. Even if not shown in the above Figures, coefficients such as C_{FZ}, C_{MY}, and C_{MZ} are also gathered in response surfaces for each trim. At first, the magnitudes of the vertical force coefficient C_{FZ} computed by *pan*MARE were met with some doubt. However, an error was not found during the investigation while it was also compared to results from a higher fidelity tool as shown in the following paragraph. This small vertical force component is assumed to be generated by the jib slope and not by any numerical error. Considering its direction and COE, this force affects mostly the pitching moment coefficient C_{MY} while the yaw moment C_{MZ} is influenced by the side force coefficient C_{FY}. Pitch and yaw moments coefficients are transformed in the VPP system and plausibility checks were conducted to detect any incorrect trend.

7.2 Sailing Conditions

To finally compare the previous aerodynamic IMS model with the new *pan*MARE points in the respective response surfaces, the modified AC75 VPP model is run for an equilibrium search in two example sailing conditions. These were selected based on the highest upwind and downwind V_{MG} conditions in the VPP version with the implemented IMS model including the 30% added drive force increment. The condition has been selected from an engineering perspective as the appendages are usually optimized targeting the highest V_{MG} conditions (Tannenberg et al., 2024). For each IMS condition, the respective updated equilibrium condition using the *pan*MARE model is shown in Table 3. Both with the same T_{WS} of 5.66 m s^{-1} (11 kn), the first two are shown for the upwind case with 47.5° T_{WA} and the last two are shown for the downwind case with 140° T_{WA}.

Table 3. Selected sailing conditions: upwind & downwind.

IMS	T_{WS}	T_{WA}	A_{WS}	A_{WA}	V_{S}	V_{MG}	λ	ϕ	θ	d_{Z}
	[m s^{-1}]	[°]	[m s^{-1}]	[°]	[m s^{-1}]	[m s^{-1}]	[°]	[°]	[°]	[m]
	5.66	47.50	20.78	11.24	16.52	11.05	0.54	0.00	0.00	-0.80
	τ	M_{TV}	M_{RA}	M_{HR}	J_{TV}	J_{HR}	δ_f	γ	δ_r	δ_e
	[-]	[-]	[°]	[-]	[-]	[-]	[°]	[°]	[°]	[°]
	0.34	-	-	-	-	-	-0.44	25.00	0.25	-2.38
***pan*MARE**	T_{WS}	T_{WA}	A_{WS}	A_{WA}	V_{S}	V_{MG}	λ	ϕ	θ	d_{Z}
	[m s^{-1}]	[°]	[m s^{-1}]	[°]	[m s^{-1}]	[m s^{-1}]	[°]	[°]	[°]	[m]
	5.66	47.50	19.49	12.64	15.16	10.29	-0.22	0.00	0.00	-0.80
	τ	M_{TV}	M_{RA}	M_{HR}	J_{TV}	J_{HR}	δ_f	γ	δ_r	δ_e
	[-]	[-]	[°]	[-]	[-]	[-]	[°]	[°]	[°]	[°]
	-	37.02	0.00	0.00	20.00	12.00	-1.51	25.00	-0.03	-1.57
IMS	T_{WS}	T_{WA}	A_{WS}	A_{WA}	V_{S}	V_{MG}	λ	ϕ	θ	d_{Z}
	[m s^{-1}]	[°]	[m s^{-1}]	[°]	[m s^{-1}]	[m s^{-1}]	[°]	[°]	[°]	[m]
	5.66	140.00	15.87	13.09	19.83	-15.24	0.21	0.00	0.00	-0.80
	τ	M_{TV}	M_{RA}	M_{HR}	J_{TV}	J_{HR}	δ_f	γ	δ_r	δ_e
	[-]	[-]	[°]	[-]	[-]	[-]	[°]	[°]	[°]	[°]
	0.51	-	-	-	-	-	-0.52	25.00	0.06	-1.46
***pan*MARE**	T_{WS}	T_{WA}	A_{WS}	A_{WA}	V_{S}	V_{MG}	λ	ϕ	θ	d_{Z}
	[m s^{-1}]	[°]	[m s^{-1}]	[°]	[m s^{-1}]	[m s^{-1}]	[°]	[°]	[°]	[m]
	5.66	140.00	14.13	15.91	17.96	-13.63	-0.65	0.00	0.00	-0.80
	τ	M_{TV}	M_{RA}	M_{HR}	J_{TV}	J_{HR}	δ_f	γ	δ_r	δ_e
	[-]	[-]	[°]	[-]	[-]	[-]	[°]	[°]	[°]	[°]
	-	42.92	-2.00	40.00	20.00	12.00	-0.46	25.00	-0.49	-0.81

All sail trim parameters beside M_{TV} have been optimized searching for maximum boat speed and the resulting values are listed in Table 4. The four conditions are computed with 0 degrees heel angle, 0 degrees pitch angle, and a fixed ride height of 0.8 m. Different from what one would have expected, with the above-presented data sets, both updated *pan*MARE conditions show less boat speed V_{S} and less V_{MG} compared to the original IMS conditions. These divergences are significant as they vary between 2-3.5 kn which for an AC75 are absolutely critical. Less boat speed means also the A_{WA} computed by the VPP with *pan*MAREs data, are both larger compared to the IMS ones. In terms of leeway angles, the new conditions show negative λ values for both updated conditions which in theory suggest less aerodynamic side force and hence plausible values. However, it must be considered that leeway profiles of an AC75 not only depend on the sail plan but are also strongly coupled with the main appendage. Its design and cant trim provide the required side force balance. Analyzing the behavior of power handles τ for the IMS and M_{TV} for the *pan*MARE models across the upwind and the downwind conditions, it can be seen that in both cases more power is required for the downwind condition compared to the upwind condition as one would expect. The upwind equilibrium main trim has 3.81% camber foot, 0 % camber head and 7.45° mid-twist while the jib shows 1.95% camber foot, flat head batten and 6.21° mid-twist. For the downwind equilibrium trim, the main has 4.49% camber foot, 2.85 % camber head and 4.36° mid-twist while the jib shows 4.05% camber foot, flat head batten, and 8.43° mid-twist. The respective sail trims can be visualized in the Figure below.

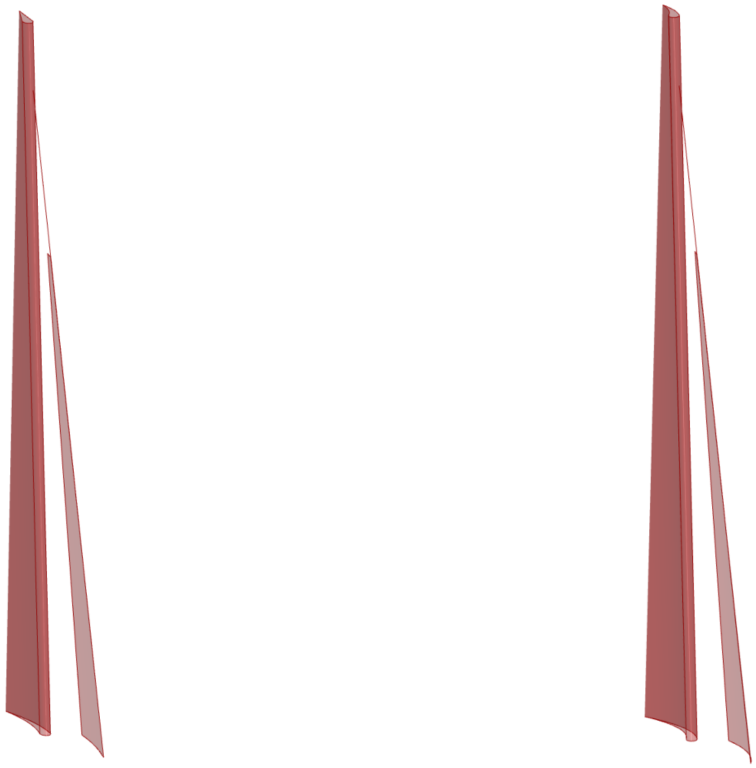

Figure 18. Equilibrium main and jib trims for (a) upwind condition and (b) downwind condition.

While it must be kept in mind that flap, rudder, and elevator angles are not directly comparable due to the different sailing speeds and angles some observation can be done on their trends between IMS and *pan*MARE. For example, significantly smaller, and even negative, rudder angles δ_r for the *pan*MARE sets suggest decreased yaw moments which is consistent with the noted side force trend. The variation of flap angles δ_f depends on the, even if light, vertical force component of the sail plan and on boat speed differential. Its behavior complies and also influences the elevator angle δ_e which is responsible for target pitch angle adjustment, set to 0 degrees.

Even if less boat performance in terms of speed and V_{MG} is achieved using *pan*MARE coupled to an articulated AC75 parametric sails model, this developed methodology is still more accurate than the empirical modified IMS coefficients considering the number of sail trims and an unbiased drive force. It is herewith also important to note that the performance divergences can be actually proven to be beneficial. Initially, the model was validated in Tannenberg et al. (2023) considering the drive force increment of 1.3 optimal. However, following several modifications implemented in the lifting line method employed for the hydrodynamic appendages, the boat performance has increased significantly using the same IMS force module. Therefore, maintaining a lower drive force coefficient for the sail plan could ensure more accuracy in predictions.

7.3 Validation Sails

In the following paragraph, coefficients of a specific sail trim computed by *pan*MARE are compared for validation with the RANS code implemented in STAR-CCM+ version 18.04. The upwind trim was selected for comparison as viscous effects are expected to be larger on the downwind equilibrium trim considering the A_{WA} magnitudes. Figure 19 reveals a comparison of the coefficient of pressure C_{P} distribution on the leeward side of the AC75 sails, left for *pan*MARE and right for STAR-CCM+.

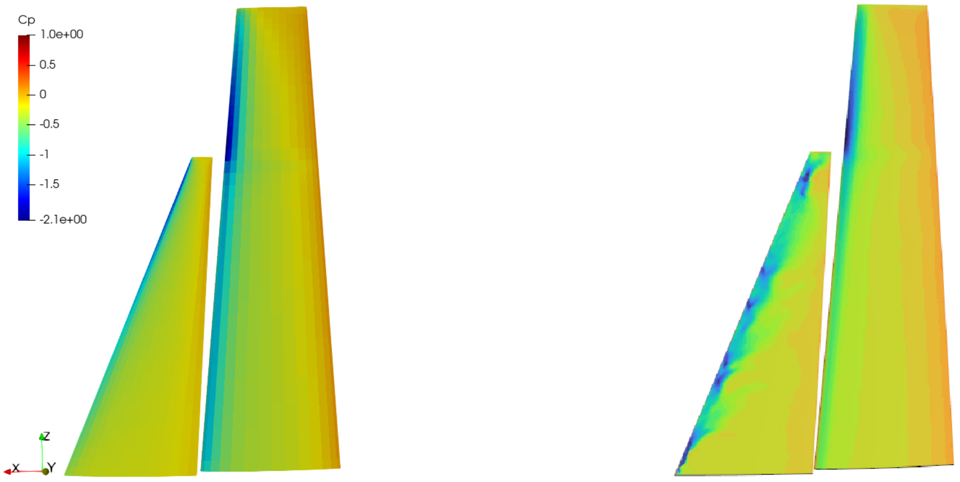

(a) **(b)**

Figure 19. C_{P} Distribution for (a) *pan*MARE and (b) STAR-CCM+: $A_{\mathrm{WA}} = 12.64°$ and $A_{\mathrm{WS}} = 19.49$ m s^{-1}.

As designed in the simplified parametric model, the leading edge of the jib is very thin, sharp, and sloped along the forestay. Figure 19(b) reveals that the airflow separates beginning from the leading edge on the leeward side with an A_{WA} of 12.64 degrees and A_{WS} of 19.49 m s^{-1}. This behavior can be perhaps reasoned also by not considering any sail deformation and by the poor trim abilities of the parametric model, especially for the jib. Already validated with the test cases, and mostly due to its larger thickness close to the leading edge, no separation was noticed on the double-skin main. Since flow separation is not accounted for by *pan*MARE large divergences occur between the potential-based and the finite volume method as listed below.

Table 4. Upwind coefficients comparison for upwind condition: *pan*MARE and STAR-CCM+.

	C_{FX}[-]	C_{FY}[-]	C_{FZ}[-]	C_{MX}[-]	C_{MY}[-]	C_{MZ}[-]
*pan*MARE	0.084	0.558	0.020	-6.671	1.062	-0.384
STARCCM+	0.049	0.563	0.024	-5.593	0.722	-0.341

A further uncertainty of these results is the mesh size and refinements required by the two different methods to converge. The divergences are excessively large in order to consider *pan*MARE a truly valid option for thin sails and further work needs to be conducted, for example, implementing a leading edge vortex correction. To confirm flow separation, a simulation with a low y^+ method can be used.

7.4 Sails & Hull Simulations

Finally, considering the aim of this project, a simulation was run in *pan*MARE for the upwind equilibrium sail trim endplating it on the implemented hull body. The focus of this section is to highlight the variation of force and moment coefficients of sails only with hull interaction under different wake settings and foiling conditions. The combined mesh was generated in CAD Rhino while still using the same chord- and span-wise distributions used in *pan*MARE for sails-only simulations for better comparison. Before proceeding with this investigation, a wake study on the hull body was conducted for A_{WA} 12.64° and A_{WS} 19.49 m s^{-1} to ensure similar behavior with the analysis conducted in Section 4. As for the hull-only simulations, gradient computation was suppressed on sharp edges such as bustle and transom. Considering the hull geometry and sail positions, some adjustments were required compared to the sails-only simulation for wake initialization and deformation. For example, on the lowest trailing edge panels of the main and jib, the wake interacts strongly or eventually collides with the hull body panels. These errors have to be taken into account and several approaches were considered: excluding the lowest sail panels for wake initialization or adjusting the wake deformation. Both approaches and the respective in C_{P} distributions are shown in Figure 20. However, focusing only on variations of force and moment coefficients, both cases showed convergence stability.

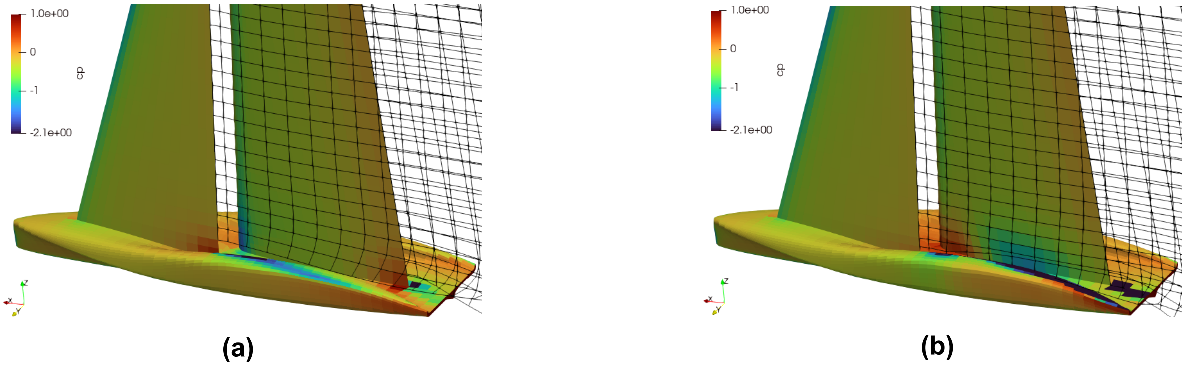

(a)

(b)

Figure 20. Two approaches for wake initialization on sails foots: $A_{\mathrm{WA}} = 12.64°$ and $A_{\mathrm{WS}} = 19.49$ m s^{-1}.

As underlined by Figure 20 above, the pressure distribution on the hull body underlines a larger solution error for the fully initialized wake compared to the other case with a missing lower wake panel. Larger pressure gradients are observed on the leeward side pod and hence the sail wake was shortened for the following simulation studies. To better accommodate the shedding vortices from the sails foots, it would be necessary to dynamically generate a body grid based on the flow conditions and the resulting vortex configuration. This adaptive mesh configuration is not implemented yet in *pan*MARE, which also lacks a method accounting for the interaction between wake and lifting panels. In the sails simulations without the implemented hull, a simplified approach was used defining a symmetry plane to endplate the sails foots. While this approach has proven to be quite useful, it also comes with modeling errors overpredicting the efficiency of the sail plan. In the following simulation, the sails are endplated to the hull's deck while the symmetry plane is defined to model the waterplane. By endplating both sails, these acquire the same foot spline geometry of the deck and hence gain sail surface compared to the horizontal foot used in the previous simulations. Considering also the mast extension, the increment of sail surfaces consists of 4.51 m^2 for the mainsail and 1.09 m^2 for the jib. With an identical simulation setup, by means of sail trim, ride height, time step, iteration numbers, etc, the results with simple symmetry endplate and hull endplate are compared in Table 5. Sails coefficients were normalized with the respective projected area and dynamic pressure.

Table 5. Coefficients comparison in $A_{\text{WA}} = 12.64°$ and $A_{\text{WS}} = 19.49$ m s^{-1}: symmetry and hull endplate.

	C_{FX} [-]	C_{FY} [-]	C_{FZ} [-]	C_{MX} [-]	C_{MY} [-]	C_{MZ} [-]	$C_{\text{FX}}/C_{\text{FY}}$ [-]	$C_{\text{FX}}/C_{\text{MX}}$ [-]
Symmetry endplate	0.084	0.558	0.020	-6.671	1.062	-0.384	0.150	-0.0125
Hull endplate	0.071	0.496	0.0252	-5.902	0.919	-0.369	0.143	-0.0120

According to Table 6, for the same A_{WA} and A_{WS}, the majority of the force and moment coefficients decrease for the hull endplate compared to the symmetry endplate. In the hull endplate case, the sail plan shows a lower drive-to-side force ratio and a lower drive force to heeling moment ratio which both underline a loss of efficiency for the hull endplated sail plan. Just as in the sails-only simulations, the trend and magnitudes of the vertical force are still questioned as only a small vertical lift is expected to be generated by sails. At target pitch, the hull body is expected to generate mostly down-force as a vertical force component. In terms of overall side force, the component generated by the hull body is expected to be relatively low compared the sails side force. However, it is known that the hull can noticeably increase the lift force of the sails, depending on hull shape, ride height, and the effectiveness of the hull as a lifting body. Within Section 4, an analysis was conducted to study wake-shedding behavior on the implemented AC75 hull body. While this investigation was conducted for several upwind cases showing similar wake behavior, it has been done for hull body only, neglecting how the sails would divert the flow on the deck; this needs to be considered in the interpretation of the results. For the combined sails and hull simulations, as shown in Figure 21, the wake shedding from the inboard windward pod edge was not mirrored as it would collapse on the mainsail panels. Considering their small impact, the wake shedding from leeward aft chine and leeward outboard pod was not implemented. The implemented shedding wakes of the bustle keel and transom top deck were not deformed while sail wakes required an adjusted desingularization factors to avoid knots.

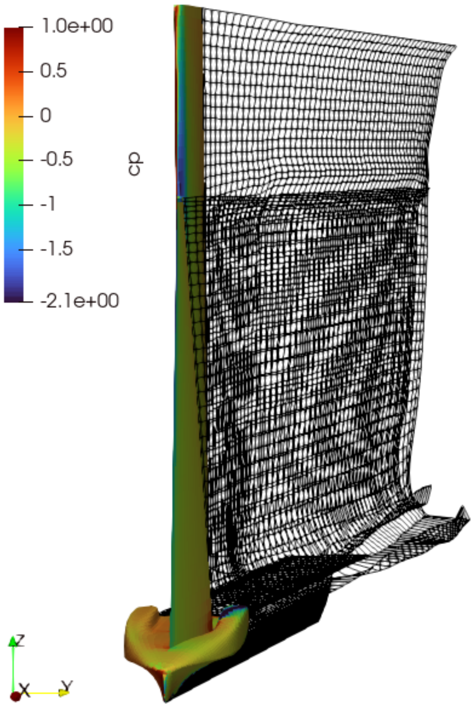

Figure 21. Wake systems of sails & hull simulation: $A_{\text{WA}} = 12.64°$ and $A_{\text{WS}} = 19.49$ m s^{-1}.

Overall, the incorporation of wakes attached to the edges of hull panels, combined with closely positioned sails and their respective wakes, appears to be effective. To roughly estimate the accuracy of this model, the magnitude of the total heeling moment is monitored in *pan*MARE at a fixed point measured at waterline height. It is known that an AC75 in an average upwind condition produces approximately -300 kNm of heeling moment. This shows an overall agreement with -312 kNm in the model with attached hull wakes.

In the following several sensitivity checks are reported focusing on sail coefficients to understand whether the *pan*MARE setup can reproduce any expected trends of forces and moments coefficients over different ride height, heel, and pitch angles. Table 7, 8 and 9 report the coefficient deltas with different values of respectively d_{Z}, ϕ and θ. A default initial sailing condition with 1 m ride height d_{Z}, 0° heel ϕ and 0° pitch θ is shown in each first column. To conduct these tests, the ride height was set high enough to avoid any intersection between hull panels and waterplane symmetry. Negative heel angles indicate windward heel while positive pitch angles stand for bow-down pitch. The environmental conditions, in terms of A_{WA} and A_{WS}, were now set identical to the hull only testcase presented in Section 4 considering the hull wake study. An A_{WA} of 14.64° and an A_{WS} of 20.98 m s^{-1} with constant wind gradient over height were used for all simulations. For all of these, an exemplary trim of main and jib was used. While the airflow is channeled by the deck, one of the biggest aerodynamic performance differentiators for an AC75 is the ride height. Specifically the ability of endplating the hull bustle on the waterline avoiding large airflow circulation from windward to leeward generating vortices. Different ride height values d_{Z}, measured vertically from the stern, are shown in Table 7: 1.0, 0.9, 0.8, and 0.7 m, respectively indicating clearances from the deepest bustle point to waterplane of 0.31, 0.21, 0.11, and 0.01 m. If a matrix of coefficients was implemented into a VPP for a series of ride heights, one would expect the software to choose the lowest possible ride height condition. Usual target heel angles for an AC75 are below 5 degrees and mostly windward for inducing more righting moment and hence to power up sails. However, this behavior could only be visualized within a VPP with a number of response surfaces for sail trims and heel angles. Target heel angles depend strongly on T_{WS} as in light to medium air, an AC75 aims for windward to flat heel while in stronger air the trend show more leeward heel based on race observation (America´s Cup, 2021). Also the target pitch angles of an AC75 rarely exceed 5 degrees. An AC75 mostly sails slightly bow-down pitch as pitch angles strongly influence the effective A_{OA} of the leeward hydrofoil wing and rudder. Overall this impacts more on the overall performance compared to better flow entry on deck to increase sails circulation. However, this effect can be extracted from the following analysis.

Table 6. Coefficients variation over ride height: $A_{\mathrm{WA}} = 14.64°$ and $A_{\mathrm{WS}} = 20.98$ m s^{-1}.

d_{Z}[m]	C_{FX}[-]	C_{FY}[-]	C_{FZ}[-]	C_{MX}[-]	C_{MY}[-]	C_{MZ}[-]	$C_{\mathrm{FX}}/C_{\mathrm{FY}}$[-]	$C_{\mathrm{FX}}/C_{\mathrm{MX}}$[-]
1	0.0754	0.5273	0.0295	-6.1735	0.9926	-0.3988	0.1429	-0.0122
0.9	0.0777	0.5382	0.0305	-6.2783	1.0139	-0.3830	0.1443	-0.0123
0.8	0.0782	0.5401	0.0306	-6.2984	1.0163	-0.3755	0.1447	-0.0124
0.7	0.0788	0.5417	0.0306	-6.2317	1.0181	-0.3661	0.1454	-0.0126

Table 7. Coefficients variation over windward heel angle: $A_{\mathrm{WA}} = 14.64°$ and $A_{\mathrm{WS}} = 20.98$ m s^{-1}.

ϕ[°]	C_{FX}[-]	C_{FY}[-]	C_{FZ}[-]	C_{MX}[-]	C_{MY}[-]	C_{MZ}[-]	$C_{\mathrm{FX}}/C_{\mathrm{FY}}$[-]	$C_{\mathrm{FX}}/C_{\mathrm{MX}}$[-]
0	0.0754	0.5273	0.0295	-6.1735	0.9926	-0.3988	0.1429	-0.01221
-2	0.0753	0.5248	0.0475	-6.1706	1.0002	-0.3632	0.1434	-0.01220
-4	0.0752	0.5232	0.0656	-6.1669	1.0134	-0.3248	0.1437	-0.01219
-6	0.0747	0.5170	0.0828	-6.1338	1.0140	-0.2894	0.1444	-0.01217

Table 8. Coefficients variation over bow-down pitch angle: $A_{\mathrm{WA}} = 14.64°$ and $A_{\mathrm{WS}} = 20.98$ m s^{-1}.

θ[°]	C_{FX}[-]	C_{FY}[-]	C_{FZ}[-]	C_{MX}[-]	C_{MY}[-]	C_{MZ}[-] C_{MZ}	$C_{\mathrm{FX}}/C_{\mathrm{FY}}$[-]	$C_{\mathrm{FX}}/C_{\mathrm{MX}}$[-]
0	0.0754	0.5273	0.0295	-6.1735	0.9926	-0.3988	0.1429	-0.0122
-2	0.0776	0.5325	0.0261	-6.2633	0.9994	-0.1642	0.1457	-0.0123
-4	0.0799	0.5377	0.0229	-6.3407	1.0101	0.0778	0.1485	-0.0126
-6	0.0818	0.5461	0.0198	-6.4380	1.0301	0.3122	0.1497	-0.0127

According to Table 7, decreasing ride height, the drive force, side force and heeling moment increase. The pitching moment seems to increase with approximately constant vertical force variation indicating a possible shift of effort center. Decreasing the ride height induces also a lower yawing moment. In Table 8, for more windward heel, the results in *pan*MARE show a decrease of drive force, side force and heeling moment. Within this analysis, the skepticism on the vertical force trends with more windward heel remains and hence also the increment of pitch moment is questionable. The windward heel seems also to induce a lower yaw moment. According to *pan*MARE, increasing the bow-down pitch angle results in larger drive, side force, and heeling moments. The vertical force decreases for higher pitch angles and the pitching moment increases. The yawing moment changes sign between -2 and -4 degrees from rotating the boat towards the wind to rotating away from the wind suggesting an aft shift of COE-x coordinate. However, a forward shift would appear more reasonable.

In addition to each force and moment coefficient, ratios between drive force to side force and drive force to heeling moment are shown in each Table. These ratio provide feedback regarding the efficiency of each sailing condition and hence the boat performance. To better understand the listed trends of Table 7, 8 and 9, Figure 22 provides plots of the ratios for each parameter variation. All three curves originate from the same point, corresponding to the default sailing condition.

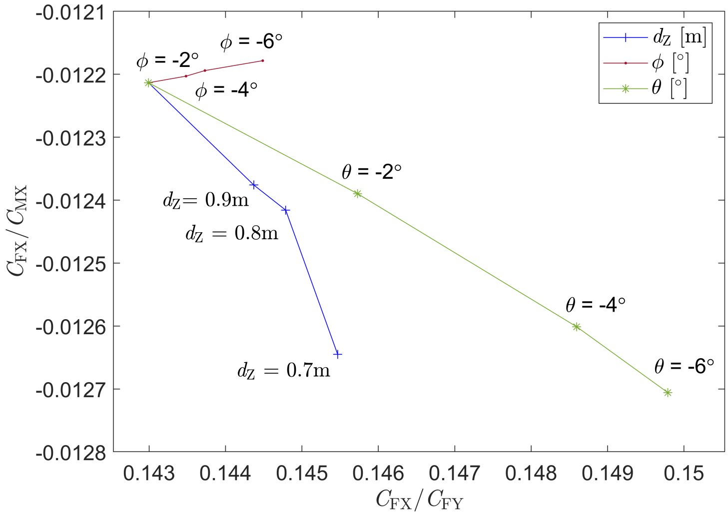

Figure 22. Coefficient ratios variation with ride heights, heel angles and pitch angles.

The plots suggest several gains, which have to be ultimately confirmed by a VPP. At lower ride heights, the drive-to-side force ratio increases, though the increment is less pronounced compared to the effect observed with larger bow-down pitch angles. Furthermore, the ratio exhibits an even smaller increase with windward heel. The drive-to-heeling moment ratio exhibits a more pronounced decrease reducing ride height, indicating a performance improvement. Conversely, the ratio decreases at a slower rate with increased bow-down pitch. For windward heel, the ratio appears to decrease very marginally.

8 CONCLUSIONS AND OUTLOOK

In conclusion, this study has demonstrated the capabilities of a potential-based panel code for sails application and underlines the reasons why even America´s Cup teams employ these tools in the early design stage. Given their substantial computational resources, AC teams frequently utilize higher-fidelity methods to develop surrogate models. In contrast, teams in comparable high-performance classes, such as offshore Ultime trimarans or IMOCA racing teams, often operate with significantly limited computational resources. These teams stand to benefit greatly from the proposed simplified methodology. However, its implementation for these classes must consider the increased number of hoisted headsails, broader sail trim ranges, and more unsteady sailing conditions.

Within this project development, test cases were first carried out validating *pan*MARE with literature in order to predict its uncertainties. Fewer divergencies were encountered for the thick double-skin mainsail compared to the thin jib application. To improve the aerodynamic accuracy of a previously developed VPP, a parametric model capable of generating a large number of sail trims, was written. The sail trims were processed by the potential flow solver and response surfaces were generated for the VPP. An upwind and a downwind equilibrium sailing condition were computed by the VPP showing an improvement compared to the previous conditions. The upwind sail trim was then compared with finite volume higher fidelity results revealing leading edges separation on the single skin thin jib. The ability of *pan*MARE to predict loads generated by a blunt AC75 hull body was then investigated. After conducting higher fidelity simulations, wakes and gradient suppression was applied on certain edges in *pan*MARE improving its overall pressure distribution. Finally combined sails and hull simulation were launched in *pan*MARE focusing on the deltas of sails coefficients. The overprediction on the efficiency of the horizontal symmetry plane at sail foots was demonstrated. Several studies were conducted investigating changes in sail coefficients depending on ride height, heel and pitch angles proving that sail and hull interactions significantly impact aerodynamic performance. Lower ride heights enhance larger drive-to-side force ratios, suggesting aerodynamic gains. However, considering all the DOFs of an AC75, the strong coupling between aerodynamic and hydrodynamic configuration must be kept in mind. Further validation and adjustments, particularly in modeling wake interactions and flow separation, are necessary to enhance the accuracy of the *pan*MARE model for practical application in AC75 performance optimization.

Even though uncertainties were already evaluated on hull-only and sails-only configurations, a higher fidelity simulation for combined sails and hull simulation would provide feedback on the wake shedding. To reduce the divergences with higher fidelity finite volume methods, *pan*MARE would benefit from a leading edge vortex correction method along with wake interaction corrections. To better capture sails and hull interaction, an adaptive mesh allowing to endplate the wake shedding from sails on the hull's deck can be considered appropriate.

ACKNOWLEDGEMENTS

The authors express the deepest gratitude to Dr. Michael Richelsen from North Sails for providing his expertise and finding time to advise the project. Finally, the authors thank Dipl-Ing Martin Scharf from the Institute of Fluid Dynamics and Ship Theory the supervision on *pan*MARE and Dr. Heikki Hansen from DNV for his VPP assistance in FS-Equilibrium.

REFERENCES

America´s Cup (2021). *36th America´s Cup*. URL: `https://ac36.americascup.com/en/results` (visited on 04/03/2021).

Birch-Tomlinson, W., Turnock, S. R., and Prince, M. (2022). Wingsail Profile Optimisation Using Computationally Efficient Methods. *24th Chesapeake Sailing Yacht Symposium*. Annapolis, MD, USA.

Chevalier, F. and Taglang, J. (2021). *LATEST AC75 DEVELOPMENTS ANALYSIS AC75 DESIGNS*. URL: `https://chevaliertaglang.blogspot.com/2021/02/americas-cup-ac75-designs-february-2021_1.html` (visited on 04/04/2024).

Collie, S., Fallow, B., Hutchings, N., and H., Y. (2015). Aerodynamic Design Development of AC72 Wings. *5th High Performance Yacht Design Conference*. Auckland, NZ.

Deperrois, A. (2021). *Flow5*. URL: `https://flow5.tech/docs/flow5_doc/flow5_doc.html` (visited on 01/10/2022).

Gambacciani, G. (2021). *AC75 Flying Hulls*. Tech. rep. Gambacciani Consulenza.

Goettsche, U. (2020). *Doctoral Thesis: Entwicklung einer numerischen Methode zur Vorhersage der hydroakustischen Schallabstrahlung von Schiffspropellern*. Tech. rep. Institute for Fluid Dynamics and Ship Theory, Hamburg Univerisity of Technology. URL: `https://tore.tuhh.de/entities/publication/4a88a64b-6d25-4963-be5d-0be58f46e60e`.

Graf, K., Renzsch, H., and Mayer, J. (2016). Prediction and Optimization of Aerodynamic Forces and Boat Speed of Foiling Catamaran with a Rig of a Rigid Wing and a Jib. *22th Chesapeake Sailing Yacht Symposium*. Annapolis, MD, USA.

Grassi, C., Foresta, M., and Lombardi G.and Katz, J. (2013). Study of Rigid Sail Aerodynamics. *Transactions of the Royal Institution of Naval Architects Part B: International Journal of Small Craft Technology* 155.1, pp. 13–24.

Hansen, H., Hochkirch, K., Burns, I., and Ferguson, S. (2019). Maneuver Simulation and Optimization for AC50 Class. *Journal of Sailing Technology* 4.1, pp. 142–160.

Hansen, H., Richards, P., and Jackson, P. (2007). Enhanced Wind Tunnel and Full-Scale Sail Force Comparison. *14th Chesapeake Sailing Yacht Symposium*. Annapolis, MD, USA.

Hochkirch, K. (2018). *FS-Equilibrium User Manual*. Tech. rep. DNV.

Institute of Fluid Dynamics and Ship Theory (2020). *panMARE (Panel Code for Maritime Applications and REsearch)*. Hamburg University of Technology. URL: `https://www.tuhh.de/panmare/code` (visited on 04/04/2024).

Katz, J. and Plotkin, A. (1991). *Low-Speed Aerodynamics*. McGraw-Hill Series in Aeronautical and Aerospace Engineering.

Masuyama, Y., Tahara, Y., Fukasawa, T., and Maeda, N. (2009). Database of Sail Shapes Versus Sail Performance and Validation of Numerical Calculations for the Upwind Condition. *Journal of Marine Science and Technology* 14.2, pp. 137–160.

Melis, M. F., Hansen, H., Fischer, M., and Abdel-Maksoud, M. (2022). Veloaddress Prediction Program for a Hydrofoiling Lake Racer. *Journal of Sailing Technology* 7.1, pp. 255–257.

Morvan, A. and Sacher, M. (2021). Efficient Jib-Mainsail Fluid-Structure Interaction Modelling based on an Extended Lifting Line Theory Validation with Semi-Rigid Sail Experiments. *7th High Performance Yacht Design Conference*. Auckland, NZ.

Patterson, J. and Binns, J. (2022). Development of a Six degrees of Freedom Veloaddress Prediction Program for the Foiling America´s Cup Vessels. *Journal of Sailing Technology* 7.1, pp. 121–152.

Paulin, A., Hansen, H., Hochkirch, K., and Fischer, M. (2015). Performance Assessment and Optimization of a C-Class Catamaran Hydrofoil Configuration. *5th High Performance Yacht Design Conference*. Auckland, NZ.

Peart, T., Aubin, N., Nava, S., Cater, J., and Norris, S. (2021). Multi-Fidelity Surrogate Models for VPP Aerodynamic Input Data. *Journal of Sailing Technology* 6.1, pp. 21–43.

Peart, T., Aubin, N., Nava, S., Cater, J., and Norris, S. (2022). Selection of Existing Sail Designs for Multi-fidelity Models. *Journal of Sailing Technology* 7.1, pp. 33–51.

Rodriguez, R., Wang, Y., Ozanne, J., Sumer, D., D., F., and Soudbakhsh, D. (2022). Adaptive Takeoff Manuever Optimization of a Sailing Boat for America´s Cup. *Journal of Sailing Technology* 7.1, pp. 21–43.

Rousselon, N. (2020). *Optimization for Sail Design*. Tech. rep. Cape Horn Engineering. URL: `https://www.cape-horn-eng.com/wp-content/uploads/Rousselon-%20Optimization_for_sail_design.pdf`.

Royal-New-Zealand-Yacht-Squadron-and-Royal-Yacht-Squadron (2022). *AC75 Class Rule*. URL: `https://www.americascup.com/files/m5498_AC75-Class-Rule-v20.pdf` (visited on 10/15/2023).

Schlichtling, H. (1978). *Boundery-Layer Theory*. Vol. 7th. McGraw-Hill Series in Aeronautical and Aerospace Engineering.

Schmitt, P., Ferreira-Gonzales, D., Goettsche, U., Schulz, C., S., N., Scharf, M., M., A.-M., and Kregting, L. (2018). Force on a Submerged Sub Sea Tidal Kite in Surface Proximity. *6th European Conference on Computational Mechanics (ECCM 6)*. Glasgow, UK.

Smith, R. W. and Wright, J. A. (2021). Simulation of the Aerolastostatic Characteristics of an America´s Cup AC75 Mast/Mainsail System. *AIAA SciTech Forum 2021, McGraw-Hill Series in Aeronautical and Aerospace Engineering*. San Diego, USA.

Smith, R. W. and Wright, J. A. (2022). Calculation of Equilibrium Sail Shapes and Integrated Aerodynamic Properties for an America's Cup AC75 Mast/Mainsail System. *AIAA SciTech Forum 2022, McGraw-Hill Series in Aeronautical and Aerospace Engineering*. San Diego, USA.

Tannenberg, R., Hochkirch, K., Walther, A., Turnock, S. R., and Boyd, S. (2024). Development of an Adjoint VPP-Driven Hydrofoil Optimisation Framework. *8th High Performance Yacht Design Conference*. Auckland, NZ.

Tannenberg, R., Turnock, S. R., Hochkirch, K., and Boyd, S. (2023). VPP Driven Parametric Design of AC75 Hydrofoils. *Journal of Sailing Technology* 8.1, pp. 162–183.